Electromagnetic and Mechanical Modeling of Large Phased Arrays of Structurally Embedded Waveguides

Nicholas J. Albertson

Thesis submitted to the Faculty of the

Virginia Polytechnic Institute and State University

in partial fulfillment of the requirements for the degree of

Master of Science

in

Aerospace Engineering

Robert A. Canfield, Chair

Mayuresh J. Patil

Majid Manteghi

December 18, 2017

Blacksburg, Virginia

Keywords: SWASS, structurally embedded antennas, multi-fidelity modeling, phased arrays

Electromagnetic and Mechanical Modeling of Large Phased Arrays of Structurally Embedded Waveguides

Nicholas J. Albertson

(ABSTRACT)

Use of Slotted Waveguide Antenna Stiffened Structures (SWASS) in future commercial and military aircraft calls for the development of an airworthiness certification procedure. The first step of this procedure is to provide a computationally low-cost method for modeling waveguide antenna arrays on the scale of an aircraft skin panel using a multi-fidelity model. Weather detection radar for the Northrop Grumman X-47 unmanned air system is considered as a case study. COMSOL Multiphysics is used for creating high-fidelity waveguide models that are imported into the MATLAB Phased Array Toolbox for large-scale array calculations using a superposition method. Verification test cases show that this method is viable for relatively accurate modeling of large SWASS arrays with low computational effort. Additionally, realistic material properties for carbon fiber reinforced plastic (CFRP) are used to create a more accurate model. Optimization is performed on a 12-slot CFRP waveguide to determine the waveguide dimensions for the maximum far-field gain and separately for the maximum critical buckling load. Using the two separate optima as utopia points, a multi-objective optimization for the peak far-field gain and critical buckling load is performed, to obtain a balance between EM performance and structural strength. This optimized waveguide is then used to create a SWASS array of approximately the same size as an aircraft wing panel using the multi-fidelity modeling method that is proposed. This model is compared to a typical conventional weather radar system, and found to be well above the minimum mission requirements.

Electromagnetic and Mechanical Modeling of Large Phased Arrays of Structurally Embedded Waveguides

Nicholas J. Albertson

(GENERAL AUDIENCE ABSTRACT)

Antennas used in military and commercial aircraft have traditionally been designed independently from the aircraft structure. Increasingly, effort has been made to integrate these processes, in order to create more efficient, dual-purpose structures. Slotted waveguide antennas, hollow rectangular tubes with slots cut in one face, are commonly used to create arrays for aircraft on-board weather radar. A type of structurally embedded antenna, slotted waveguide antenna stiffened structures (SWASS), consists of slotted waveguides that are sandwiched between two layers of a composite material. This sandwich structure can be used in place of the conventional structure used for aircraft skin, allowing the slotted waveguides to function not only as antennas, but also as part of the aircraft's load-bearing structure. Because of the geometric complexity of the slotted waveguides, generating accurate models of the antenna performance can be difficult and requires a great deal of computational power. This thesis presents and validates a method for reducing the complexity of modeling the antenna performance of SWASS arrays. Additionally, optimizations are performed to improve both the waveguide's performance as an antenna and as a load-bearing part of the aircraft structure. Finally, the optimized SWASS array is compared to the actual mission requirements of the Northrop Grumman X-47 unmanned aircraft, and is found to perform above the required levels.

Dedicated to my wonderful wife Lyndsey, without whom none of this would have been possible.

Acknowledgments

I would like to thank Dr. Canfield for his support of me throughout my graduate career from the very beginning. He signed on to be the advisor for a student who was a novice to the electrical engineering to work on a project that deals heavily with antennas. Though neither of us was an expert, he guided me through the difficulties of jumping into a wholly unknown field to expand the boundaries of my multidisciplinary design capabilities.

I would also like to gratefully acknowledge Mr. Robert J. Hanley, Director, USN & USMC Airworthiness and CYBERSAFE Office, AIR-4.0P. This research was funded in part by prime contract #HC1047-05-D-4005, purchase order APSC01797, clearance statement A10160-S166-PR01. Additionally, special thanks are given to Katie Hauck and Doug Pennock of the NAVAIR Radar and Antenna Systems Division (4.5.5.2) and to Rick Ryan of the NAVAIR Tactical Aircraft Strength Division (4.3.3.1) for their technical advice.

Contents

List of Figures ix

List of Tables xiii

1 Introduction 1

1.1 Motivation 3

1.2 Research Objectives 4

1.3 The State of the Art 5

1.4 Thesis Organization 8

2 EM Modeling of Large Phased Arrays of Structurally Embedded Waveguides 10

2.1 Introduction 10

2.2 Methods 15

2.2.1 Waveguide Theory 15

2.2.2 RF Model for WR90 Slotted Waveguide Antenna 19

2.2.3 Array Gain Calculation Using Superposition 21
2.2.4 Verification With Realistic Material Properties - CFRP 25
2.2.5 Waveguide RF Performance Optimization 29
2.2.6 SWASS Panel Evaluation 33
2.3 Results 33
2.3.1 Superposition Verification 33
2.3.2 CFRP Material Properties Verification 39
2.3.3 Waveguide EM Optimization 40
2.3.4 Large Array Modeling 42
2.4 Conclusion and Future Work 44

3 Structural Design Methods for SWASS **50**

3.1 Waveguide Structural Performance Optimization 51
3.1.1 Coarse Optimization Proof of Concept 51
3.1.2 High-Fidelity Optimization 57
3.2 Multi-Objective Optimization 58
3.3 SWASS Panel Evaluation 59

4 Results **60**

4.1 Waveguide EM Optimization (Chapter 2 Review) 60
4.2 Waveguide Structural Performance Optimization 61

4.2.1 Coarse Optimization Proof of Concept 61

4.2.2 High-Fidelity Optimization 63

4.3 Multi-Objective Optimization 68

4.4 SWASS Panel Evaluation 72

5 Conclusions & Summary **75**

5.1 Summary of Technical Contributions 79

5.2 Recommendations for Future Work 80

Bibliography **81**

List of Figures

1.1 Examples of aircraft antennas. (a) Mechanically steered slotted waveguide antenna array under a radome [19], (b) externally mounted blade antenna [20], and (c) Airborne Warning and Control System (AWACS) antenna[21] . 3

1.2 Northrop-Grumman X-47 with embedded SWASS array[1] 4

1.3 Waveguide design variables [8] 7

1.4 Four SWASS design concepts for highest strength-to-weight ratio[8] 9

2.1 Northrop-Grumman X-47 with embedded SWASS array [8, 12, 22] 14

2.2 Waveguide design variables [8, 13] 16

2.3 Far-field gain pattern of a four-slot waveguide 19

2.4 Four-slot waveguide CAD model (a) and its mesh (b) 20

2.5 Four-slot waveguide shown with simulation domain 21

2.6 COMSOL high-fidelity model of a single waveguide element [8, 13] 23

2.7 COMSOL high-fidelity model of a three-element waveguide array 23

2.8 Nine-element waveguide array 24

2.9 COMSOL high-fidelity model of a long waveguide array 25

2.10 Single waveguide far-field gain (dB). COMSOL high-fidelity (a) front and (b) side views. (c) Front and (d) side views after importing to MATLAB. 35

2.11 Three waveguide array far-field gain (dB). (a) COMSOL high-fidelity and (b) MATLAB superposition 36

2.12 9-Waveguide array far-field gain (dB). (a) Superposition of three 1x3 arrays and (b) superposition of 9 single elements. 37

2.13 Single long 12-slot waveguide far-field gain (dB). COMSOL high-fidelity (a) front and (b) side views. 38

2.14 Genetic Algorithm Convergence Plot 41

2.15 Waveguide geometric configurations (a) before and (b) after genetic algorithm optimization 43

2.16 Far-field gain patterns before and after coarse genetic algorithm optimization. Waveguide with nominal dimensions (a) front and (b) side views. Waveguide with EM-optimized dimensions (c) front and (d) side views. 46

2.17 Nelder-Mead Convergence Plot 47

2.18 Waveguide geometric configurations (a) before and (b) after Nelder-Mead optimization 47

2.19 Far-field gain patterns before and after high-fidelity Nelder-Mead optimization. Waveguide with nominal dimensions (a) front and (b) side views. Waveguide with optimized dimensions (c) front and (d) side views. 48

2.20 40-waveguide SWASS array far-field gain patterns before and after high-fidelity EM optimization. Array consisting of waveguides with nominal dimensions (a) front and (b) side views. Array of dual-optimized waveguides (c) front and (d) side views. 49

3.1 Waveguide cross section divided into sections (i=1...4) for moment of inertia calculation 53

3.2 Typical waveguide upper surface membrane mesh 54

3.3 Von Mises stress distribution for the waveguide with nominal dimensions . . 54

3.4 Shell mesh used for high-fidelity structural optimization 58

4.1 Iteration history for (a) SAO and (b) SQP optimizations. 62

4.2 Stresses in top surface of waveguide with optimal dimensions determined by coarse optimization. Element 22 is highlighted. 63

4.3 Design space slice showing critical buckling load contours versus slot width and length 64

4.4 Design space slice showing critical buckling load versus waveguide width and height 65

4.5 Iteration history for high-fidelity structural optimization 66

4.6 (a) Nominal and (b) structurally optimal waveguide configurations 67

4.7 Multi-Objective Optimization Iteration History 69

4.8 Multi-Objective Optimization Objective Function History 70

4.9 (a) Nominal, (b) structurally optimized, (c) EM optimized, and (d) dual-optimized waveguide configurations 71

4.10 Far-field gain (dB) patterns before and after high-fidelity multi-objective optimization. Waveguide with nominal dimensions (a) front and (b) side views. Waveguide with dual-optimized dimensions (c) front and (d) side views. . . . 73

4.11 40-waveguide SWASS array far-field gain (dB) patterns before and after high-fidelity multi-objective optimization. Array consisting of waveguides with nominal dimensions (a) front and (b) side views. Array of optimized waveguides (c) front and (d) side views. 74

List of Tables

2.1 Nominal Slotted Waveguide Dimensions 17

2.2 Test Case 2 Peak Gain Error 34

2.3 Test Case 3 Peak Gain Error 37

2.4 Coarse EM Optimization - Optimum Waveguide Dimensions 42

2.5 High-Fidelity EM Optimization - Optimum Waveguide Dimensions 42

3.1 Material properties of copper 52

3.2 Material properties of CFRP 57

4.1 Optimum values of design variables - coarse structural optimization 62

4.2 Optimum Slotted Waveguide Dimensions - High-Fidelity Structural Optimization 67

4.3 Optimum Slotted Waveguide Dimensions - Multi-Objective Optimization . . 69

5.1 Comparison of three optimized configurations with nominal configuration . . 77

Nomenclature

AF	Array factor
A_i	Area of section i, m^2
b_i	Base dimension of section i, m
c_i	Y-axis centroid of section i, m
d_1	Slot width, m
d_2	Slot length, m
d_3	Slot spacing from centerline, m
d_4	Longitudinal slot spacing, m
d_5	Waveguide width, m
d_6	Waveguide height, m
d	Center-to-center distance of waveguides in array, m
E	Electric field, V/m
$\overline{E}$	Young's modulus
E_p	Electric field evaluated at point p on surface S, V/m
G	Peak far-field gain, dB
h_i	Height dimension of section i, m
H	Magnetic field, A/m
I	Current supplied to element, A
$\overline{I}$	Waveguide moment of inertia, m^4
k_0	Free space wave number
L	Waveguide length, m
M	Waveguide mass, kg
M_0	Nominal waveguide mass, kg
$\hat{n}$	Unit normal vector to waveguide surface
n	Number of slots in element
N	Number of elements in array
P	Compressive applied load, N
P_{cr}	Critical buckling load, N
r	Radius vector of surface S, m

r_0	Unit vector pointing from origin to point p
S	Surface of sphere for evaluating E
t	Waveguide wall thickness, m
t_u	Equivalent smeared waveguide wall thickness, m
y	Location of waveguide neutral axis, m
α	Inter-element phase shift in array, rad
β	Phase constant, rad/m
η_0	Free space impedance, Ω
θ	Beam steering direction, rad
λ_0	Free space wavelength, m
λ_c	Cutoff wavelength, m
λ_g	Guided wavelength, m
ρ	Waveguide material density, kg/m^3
σ	Yield stress, MPa
σ_x	x-component of normal stress, MPa
σ_y	y-component of normal stress, MPa
τ_{xy}	Shear stress, MPa
σ_{VM}	Von Mises stress, MPa

Chapter 1

Introduction

In aviation, it is the general practice to strive for the lightest, strongest, and fastest aircraft possible. Even a small improvement in one of these areas could make a big difference in terms of performance or cost. For example, if a commercial airline was able to reduce the weight of each aircraft in their fleet by just a few pounds, that could mean a savings of hundreds of thousands of dollars in jet fuel costs per year. This is especially true with military aircraft, where even the slightest weight or drag savings could give a pilot the edge he needs to complete his mission safely.

Traditionally, different aircraft systems have been designed and built by specialists, where each system was designed for one purpose and had the optimum performance for that purpose. However, with the constant push for improvement, and the advent of computer aided design (CAD) and more capable optimization methods, interdisciplinary and multi-functional design has become the new norm. Following this new interdisciplinary thrust, a new type of embedded system has evolved: conformal load-bearing antenna structures (CLAS)[5]. While conventional antennas were designed and built separately from aircraft structural components, CLAS serve the dual purpose of supporting loads within the aircraft structure

and providing radio frequency (RF) communication. Although requiring more effort on the design and manufacturing side, these improved systems could allow for the large surface structure of an aircraft to be used efficiently as antennas and communications systems, leading to mission-critical weight savings and perhaps broadening the mission capabilities of the aircraft.

Conventional aircraft antennas, though performing capably as antennas, may negatively affect aircraft performance in other areas. Figure 1.1a shows a weather radar array in behind the nosecone of an aircraft. This array is bulky and must be mechanically steered, adding significant weight to the aircraft, and the large enclosing radome is structurally weak, due to the need for RF transparency. A second common type of aircraft antenna is showed in Figure 1.1b, where a blade-shaped antenna protrudes from the aircraft. This increases the overall drag of the aircraft, and can potentially lead to increased radar profile, which can be a big concern for military applications. Figure 1.1c shows the extreme case of protruding antennas, where the Airborne Warning and Control System (AWACS) antenna is used for long-range target tracking. These protruding antennas are also more prone to impact damage.

A type of CLAS, first suggested as a novel concept by Callus [6], is the Slotted Waveguide Antenna Stiffened Structure (SWASS). The initial idea for SWASS consisted of internal hat stiffeners along an aircraft's skin acting as waveguides, where the aircraft skin material is electromagnetically transparent to allow for the waves to propagate externally. This concept was not practical, as it was found that the waveguides needed to be closer together than was necessary for hat stiffeners. Callus proposed a second, more successful novel concept: using rectangular waveguide antennas as the core of a composite sandwich structure to be used in place of the usual honeycomb core. The outer moldline of the sandwich structure would have slots cut in the material to allow wave propagation, but which were to be filled with an electrically transparent substance to maintain a smooth outer moldline to preserve the

(a)

(b)

(c)

Figure 1.1: Examples of aircraft antennas. (a) Mechanically steered slotted waveguide antenna array under a radome [19], (b) externally mounted blade antenna [20], and (c) Airborne Warning and Control System (AWACS) antenna[21]

aerodynamics of the aircraft. Callus and others later successfully built and tested a SWASS array constructed entirely of carbon fiber reinforced plastic (CFRP) [7]. Previously, typical CLAS had been patch antennas for low-power applications, such as communications, whereas slotted waveguide antennas can be used for higher-power applications, such as radar. The research presented here will focus on SWASS, as outlined in the next section.

1.1 Motivation

In an effort to further understand the design and implementation challenges associated with SWASS, the Northrop Grumman X-47 unmanned combat air system [22] will be used as a case study for the notional implementation of a SWASS weather detection radar. For this application, the SWASS will be made up of WR-90 slotted waveguides that operate at a frequency of 10 GHz (X band). The X-47 is shown in Figure 1.2 with an example of an embedded SWASS. Since SWASS perform the dual purpose of providing EM communication and structural support, an accurate model of both the structural and electrical performance must be created. A multi-objective optimization will be performed to create a balance of EM performance and structural strength. The EM model will be compared against radar performance requirements of typical missions of the X-47 aircraft.

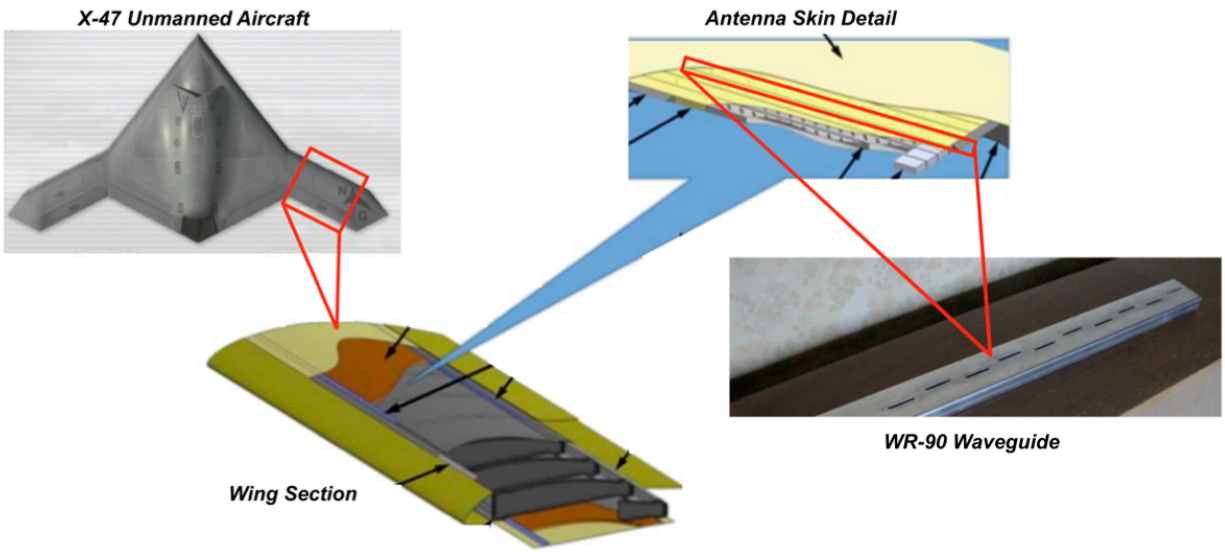

Figure 1.2: Northrop-Grumman X-47 with embedded SWASS array[1]

As this research is still at the proof-of-concept stage, some simplifications to the model are expedient. For this preliminary research, the waveguides' interference with the rest of the aircraft or with each other is neglected. Additional electrical components, such as the power supplies and backshorts are not modeled. These components may contribute some EM interference, so future research may be conducted without these assumptions.

1.2 Research Objectives

The main objective of this research is to aid the future implementation of SWASS by reducing the need for computationally expensive high-fidelity analyses with a new multi-fidelity design method, and use this method, in tandem with optimization, to generate an ideal SWASS panel model for implementation as a weather radar on the Northrop-Grumman X-47 aircraft. As SWASS are inherently multidisciplinary in nature, this design ideally would be completed while also maintaining high structural strength. Additionally, this research may contribute to an airworthiness certification process for SWASS, wherein proposed panel designs easily

could be checked against the mission requirements. A detailed survey of current SWASS literature was performed, and several gaps were identified. This has led to the following research objectives:

1. Propose and validate a multi-fidelity modeling technique for electromagnetic analysis of SWASS panels

2. Determine an optimum set of slotted waveguide dimensions that that produce the highest possible peak far-field gain, which will be used to create an electromagnetic model of a full SWASS panel

3. As structural and electromagnetic concerns motivate different design choices, perform a multi-objective optimization to simultaneously optimize the electromagnetic and structural performance to obtain the best overall SWASS panel to implement in the Northrop-Grumman X-47 aircraft.

The first two of these objectives are addressed in a separate journal article that is presented as Chapter 2 in this thesis.

1.3 The State of the Art

The Smart Skin Structures Technology Demonstration (S3TD) was the first Air Force Research Lab (AFRL) CLAS program. A multi-arm spiral antenna was embedded in an aircraft fuselage panel. The S3TD program verified that an antenna could be embedded in the structure of an aircraft body panel and bear loads, while also satisfying the electromagnetic requirements of the antenna [16]. A later AFRL CLAS program called Radio Frequency Multifunction Structure Aperture (MUSTRAP) tested two antenna designs, a multi-arm spiral

antenna embedded in the aircraft body and a blade antenna contained within the vertical tail, and provided further verification that antennas can bear loads while still adequately performing the mission requirements [3].

CLAS systems can replace traditional wire or blade antennas that protrude from the aircraft surface, resulting in reduced parasitic drag and lower radar signature. Whereas these external antennas tended to be smaller and did not add much weight, larger and bulkier antennas that were covered by radomes to reduce drag can be replaced by CLAS, resulting in significant weight savings. Smallwood et al. [23] studied the effects of bending due to aerodynamic loading on the performance of a load-bearing antenna system embedded in the wing of a joined-wing aircraft. It was found that bending of the embedded CLAS did affect the directionality of the antenna, but to a small enough degree that electronic steering adjustments could be made to compensate. Boeing performed a viability analysis for using CLAS to replace primary load-bearing structures, such as wing panels, and secondary structures, such as door panels, and determined that it would be beneficial for weight savings without compromising the strength of the structures [25]. As research continues, different types of antennas are being considered for use in CLAS, such as the bilayer log-periodic dipole antenna, built and tested by Bishop et al. [4]. Further survey of the literature in the area of electromagnetic performance of SWASS is contained within Chapter 2.

The dimensions and size of the waveguides and placement of the slots for SWASS arrays are dictated according to the desired operational frequency, as outlined by Elliott [11]. However, this procedure is a solely theoretical approach for determining the dimensions for the best overall electromagnetic (EM) performance, without regard for structural strength. In order to determine an optimum balance between structural and electrical effectiveness, it is possible that the waveguide dimensions suggested by Elliott must be changed to increase the strength. Ha and Canfield [13] performed a sensitivity study to determine which of the waveguide

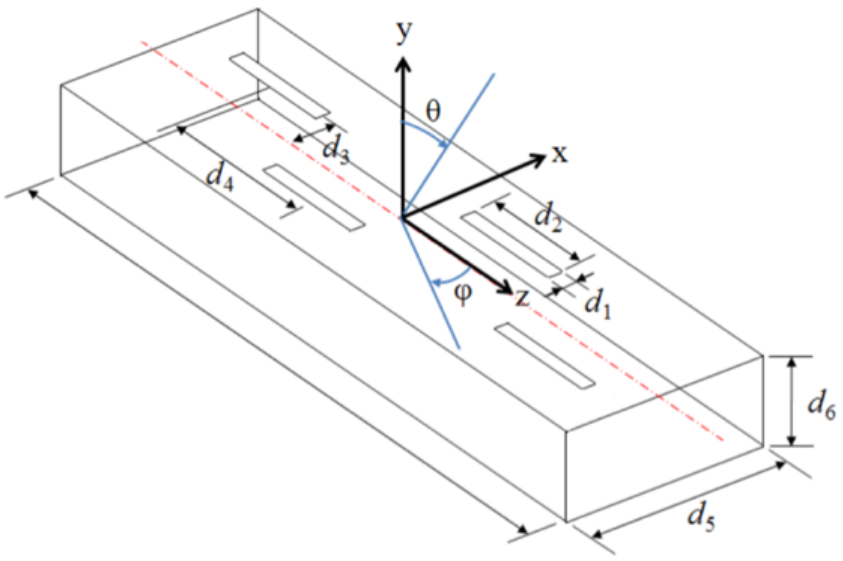

Figure 1.3: Waveguide design variables [8]

dimensions had the greatest effect on the electrical performance and which could be altered slightly in favor of increasing the waveguide strength. The waveguide dimensions, as shown in Figure 1.3, that were found to have low EM sensitivity, and could potentially be altered significantly to favor structural strength, were slot width (d_1), longitudinal slot spacing (d_4), and waveguide height (d_6). A study by Kim et al. [15] proposed several novel designs for SWASS composite sandwich structures and performed simulations and experiments to determine the configuration with the highest strength to weight ratio. The four concepts considered, shown in Figure 1.4, were:

1. Carbon fiber reinforced plastic (CFRP) slotted waveguide tubes with both top and bottom sandwich layers also made from CFRP. Because CFRP is not EM transparent, slots would also have to be cut in the outer CFRP skin to allow the EM waves to propagate. To maintain a smooth outer mold line (OML), these slots were to be filled with an EM transparent material.

2. CFRP slotted waveguide tubes with both top and bottom sandwich layers made from

EM transparent fiberglass.

3. Copper foil waveguides, which have better EM performance than CFRP waveguides, wrapped in fiberglass for structural strength, with both top and bottom sandwich layers also made from EM transparent fiberglass.

4. Copper foil waveguides wrapped in fiberglass for structural strength, with only the top sandwich layers made from EM transparent fiberglass. The inner mold line (IML) layer would be CFRP, a stronger material than fiberglass, to provide additional stiffness.

For the structural analysis of these SWASS concepts, it was proposed that an equivalent two dimensional plate be made by smearing the effects of the waveguides, slots, and laminates. This method significantly reduced computational complexity, but resulted in significant errors. Higher-fidelity structural modeling was also performed, and concept 1 was found to have the highest strength-to-weight ratio, but concept 4 was suggested as a possible compromise to increase EM performance. Experimental coupon tests were also performed, but there was uncertainty due to boundary conditions and laminate bonding strength. A combined structural and EM performance optimization study has yet to be completed, and was suggested as future work by Kim et al.

1.4 Thesis Organization

The organization of this thesis is as follows. Chapter 2 consists of a journal article entitled "Electromagnetic Modeling of Large Phased Arrays of Structurally Embedded Waveguides" that has been presented in its entirety. This article contains the first half of the research completed for this thesis, including the details of the validation of multi-fidelity modeling of SWASS and the optimization of the electromagnetic performance of SWASS. This arti-

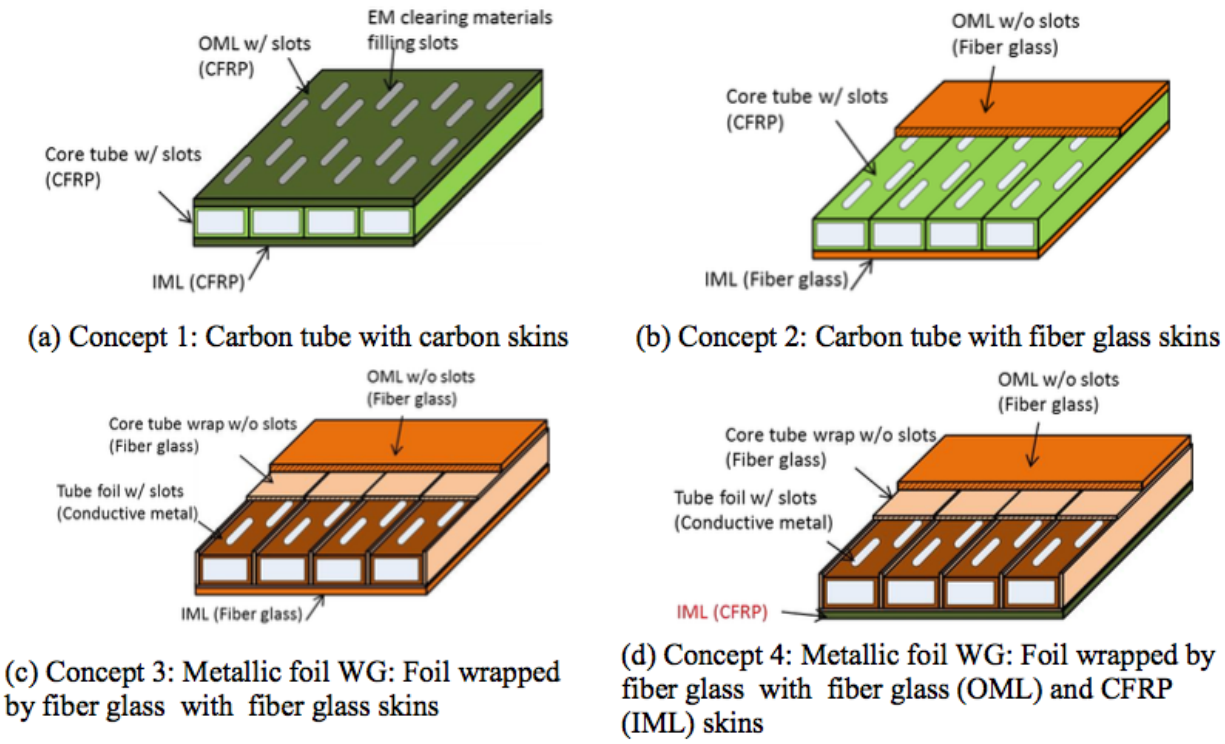

(a) Concept 1: Carbon tube with carbon skins

(b) Concept 2: Carbon tube with fiber glass skins

(c) Concept 3: Metallic foil WG: Foil wrapped by fiber glass with fiber glass skins

(d) Concept 4: Metallic foil WG: Foil wrapped by fiber glass with fiber glass (OML) and CFRP (IML) skins

Figure 1.4: Four SWASS design concepts for highest strength-to-weight ratio[8]

cle will shortly be submitted for peer review. Chapter 3 presents the methods used for the structural analysis and optimization of slotted waveguide antennas for SWASS, as well as the multi-objective optimization that balances the electromagnetic and structural performance. Chapter 4 summarizes the results from the electromagnetic optimization as laid out in Chapter 2, as well as the results of the structural and multi-objective optimizations from Chapter 3. Finally, Chapter 5 presents the conclusions and highlights the technical contribution of this research, and presents recommendations for future work.

Chapter 2

EM Modeling of Large Phased Arrays of Structurally Embedded Waveguides

2.1 Introduction

Historically, aircraft structural components have been designed and built separately from communication systems and avionics. The separation of these design processes results in lower-complexity systems, but with greater weight and lower structural efficiency than if they had been designed in concert. With the recent push towards interdisciplinary and multi-functional design, a new type of embedded antenna has evolved: Conformal Load-Bearing Antenna Structures (CLAS[5, 6]). These antennas serve the dual purpose of supporting loads within the aircraft structure and providing radio frequency (RF) communication. Although requiring more effort on the design and manufacturing side, these improved systems allow for the large surface structure of an aircraft to be used efficiently as antennas and communications systems, leading to mission-critical weight savings and perhaps broadening the missions available on any one aircraft platform.

The Smart Skin Structures Technology Demonstration (S3TD) was the first Air Force Research Lab (AFRL) CLAS program. The S3TD program verified that an antenna could be embedded in the structure of an aircraft body panel and bear loads, while also satisfying the electromagnetic requirements of the antenna [16]. A later AFRL CLAS program called Radio Frequency Multifunction Structure Aperture (MUSTRAP) tested two antenna designs, one in embedded in the aircraft body and one in the vertical tail, and provided further verification that antennas can bear loads while still adequately performing the mission requirements [3].

CLAS systems can replace traditional wire or blade antennas that protrude from the aircraft surface, resulting in reduced parasitic drag and lower radar signature. While these external antennas tended to be smaller and did not add much weight, larger and bulkier antennas that were covered by radomes to reduce drag can be replaced by CLAS, resulting in significant weight savings. Smallwood et al. [23] studied the effects of bending due to aerodynamic loading on the performance of a load-bearing antenna system embedded in the wing of a joined-wing aircraft. It was found that while the EM characteristics of the antenna arrays were altered by bending due to aerodynamic loading, the differences were small enough that compensation by electrical phasing could be accomplished. Boeing performed a viability analysis for using CLAS to replace primary load-bearing structures, such as wing panels, and secondary structures, such as door panels, and determined that it would be beneficial for weight savings without compromising the strength of the structures [25]. As research continues, different types of antennas are being considered for use in CLAS, such as the bilayer log-periodic dipole antenna, built and tested by Bishop et al. [4].

A type of CLAS, first suggested as a novel concept by Callus [6], is the Slotted Waveguide Antenna Stiffened Structure (SWASS). Previously, typical CLAS had been patch antennas for low-power applications, such as communications, whereas slotted waveguide antennas can

be used for higher-power applications, such as radar. The initial idea for SWASS consisted of internal hat stiffeners along an aircraft's skin acting as waveguides, where the aircraft skin material is electromagnetically transparent to allow for the waves to propagate externally. This concept was not practical, as it was found that the waveguides needed to be closer together than was necessary for hat stiffeners. Callus proposed a second, more successful novel concept: using rectangular waveguide antennas as the core of a composite sandwich structure to be used in place of the usual honeycomb core. The outer moldline of the sandwich structure would have slots cut in the material to allow wave propagation, but which were to be filled with an electrically transparent substance to maintain a smooth outer moldline to preserve the aerodynamics of the aircraft. Callus and others later successfully built and tested a SWASS array constructed entirely of carbon fiber reinforced plastic (CFRP) [7]. This sandwich structure is the SWASS design considered here.

The dimensions and size of the waveguides and placement of the slots for these arrays are dictated according to the desired operational frequency, as outlined by Elliott [11]. However, this procedure is a solely theoretical approach for determining the dimensions for the best overall electromagnetic (EM) performance, without regard for structural strength. In order to determine an optimum balance between structural and electrical effectiveness, it is possible that the waveguide dimensions suggested by Elliott must be changed to increase the strength. Ha and Canfield [13] and Canfield and Kim [8] performed a sensitivity study to determine which of the waveguide dimensions had the greatest effect on the electrical performance and which could be altered slightly in favor of increasing the waveguide strength. Another study by Kim et al. [15] proposed several novel designs for SWASS composite sandwich structures and performed simulations and experiments to determine the configuration with the highest strength to weight ratio. The design concept with CFRP waveguides was found to have the highest strength to weight ratio, but the concept with fiberglass-wrapped copper

foil waveguides was suggested as a possible compromise to increase EM performance. A combined structural and EM performance optimization study has yet to be completed, and was suggested as future work by Kim and Canfield.

While there has been an increase in research on CLAS systems over the last two decades, there has been no significant effort into defining a set of requirements to determine the airworthiness of an aircraft with these systems embedded in the structure. Callus [5] notes that the airworthiness certification process for CLAS will likely be more difficult than for conventional aircraft with separately designed systems, since a single CLAS component will have to be tested for both structural strength and EM performance. At present, CLAS have not been implemented on flying aircraft, but some ground tests have been performed.

Because Elliott's analytical models for the electromagnetic behavior of slotted waveguide antennas are cumbersome and are at a low fidelity that does not allow for sensitivity analysis, the finite element method (FEM) must be used. One of the challenges for developing SWASS is that it is computationally expensive to generate accurate electromagnetic models of slotted waveguide antennas for FEM, due to their geometric complexity. A method is presented here for modeling the electromagnetic performance of a SWASS panel using a multi-fidelity model that utilizes a low-complexity superposition calculation to build up an array from high-fidelity FEM models of individual waveguides. This method could be used as part of an airworthiness certification process for SWASS, to see if the panel designs meet the mission requirements.

A notional weather detection radar on Northrop Grumman's X-47 unmanned combat air system [22] will be used as a case study. For this application, the SWASS will be made up of WR-90 slotted waveguides that operate at a frequency of 10 GHz (X band). The X-47 is shown in Figure 2.1 with an example of an embedded SWASS. Since SWASS perform the dual purpose of providing EM communication and structural support, an accurate model

of both the structural and electrical performance must be created. The EM model will be compared against radar performance requirements of typical missions of the X-47 aircraft.

As this is still at the proof-of-concept stage, some simplifications to the model are required. For this preliminary research, it is assumed that the waveguide arrays do not experience any interference with the rest of the aircraft. Future research may be conducted without these assumptions. After the later addition of structural modeling, the combined electrical and structural model will be used to optimize the SWASS array for both EM performance and structural strength. However, this paper will focus only on electromagnetic modeling of SWASS.

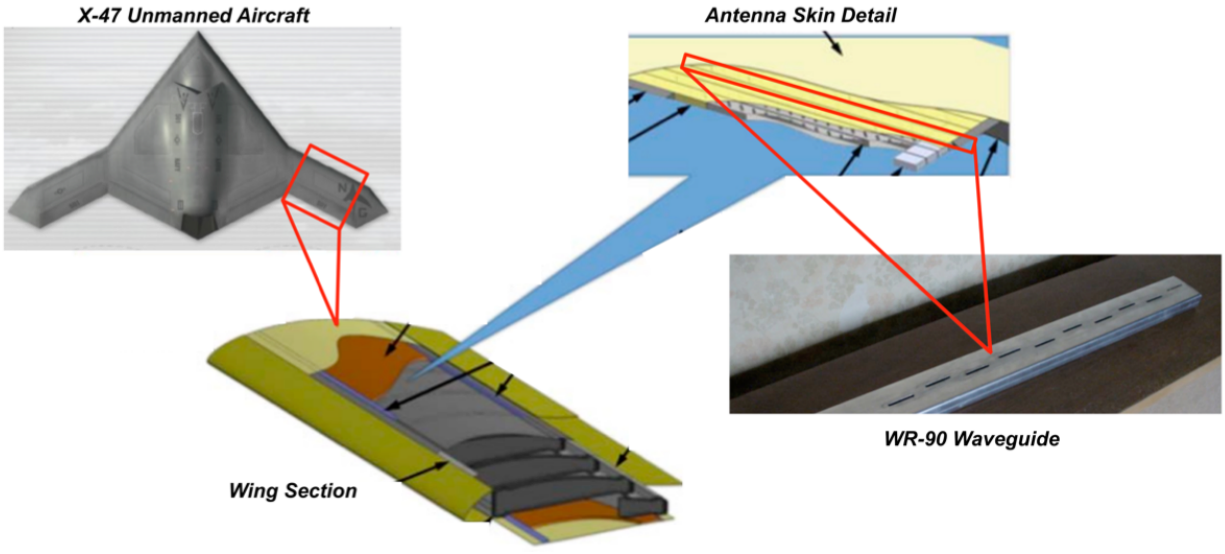

Figure 2.1: Northrop-Grumman X-47 with embedded SWASS array [8, 12, 22]

2.2 Methods

2.2.1 Waveguide Theory

Waveguides are hollow, conductive, rectangular tubes that can be used for low-loss RF signal transmission. When slots are cut into the walls of a waveguide, the signal is transmitted into free space. The ability of a waveguide to transmit and propagate a signal is highly frequency-dependent, as waveguides tend to handle very narrow frequency bands. The optimal operating frequency is dependent on the dimensions of the waveguide and the dimensions and placement of the slots, so the desired operating frequency often determines the design dimensions. The six relevant waveguide design variables are shown in Figure 2.2. These variables are slot width (d_1), slot length (d_2), slot spacing from the centerline (d_3), longitudinal slot spacing (d_4), waveguide width (d_5), and waveguide height (d_6).

Several wave propagation modes can exist within the waveguide, but since the walls are rectangular, the first transverse electric (TE10) mode dominates [8]. The TE10 mode occurs when the electric field is perpendicular to the propagation direction. The waveguide cutoff wavelength λ_c is the wavelength below which no propagation will occur. This cutoff wavelength and the free space wavelength λ_0 together are used to determine the length of the wave in the waveguide, also known as the guided wavelength λ_g:

$$\lambda_g = \frac{1}{\sqrt{\lambda_0^{-2} - \lambda_c^{-2}}} \tag{2.1}$$

The nominal values for the design dimensions were initially determined analytically by Elliott [11] in 1983, and were improved by Wade [26] in 2001. For a waveguide with n slots, the slot

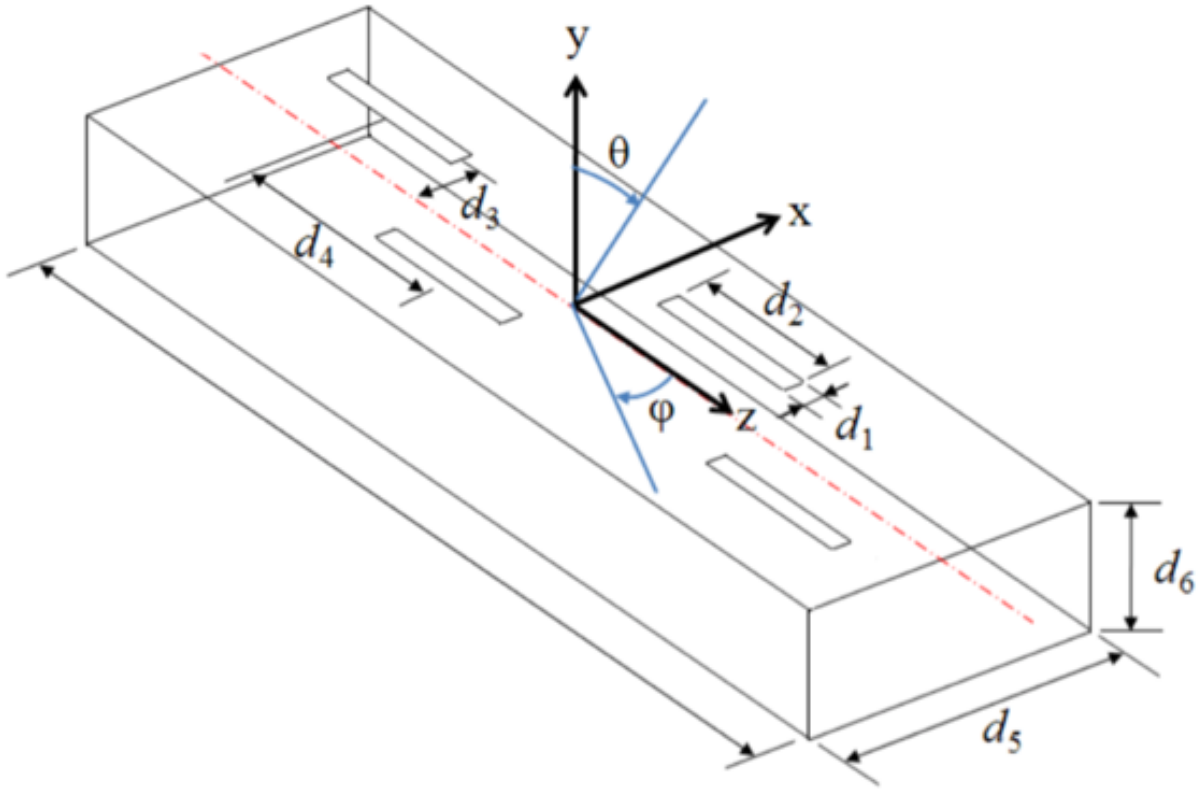

Figure 2.2: Waveguide design variables [8, 13]

Table 2.1: Nominal Slotted Waveguide Dimensions

Variable	Description	Nominal Value
d_1	Slot width	1.59 mm
d_2	Slot length	14.55 mm
d_3	Slot offset from centerline	2.14 mm
d_4	Longitudinal slot spacing	19.88 mm
d_5	Waveguide width	22.86 mm
d_6	Waveguide height	10.16 mm

dimensions are calculated using

$$d_1 = \frac{0.0625 d_6}{0.9} \tag{2.2}$$

$$d_2 = \lambda_0 \left(\frac{0.210324}{n^4} - \frac{0.338065}{n^3} + \frac{0.12712}{n^2} + \frac{0.034433}{n} + 0.48253 \right) \tag{2.3}$$

$$d_3 = \frac{d_5}{\pi} \sqrt{\arcsin\left(2.09n \left(\frac{\lambda_g}{\lambda_0}\right) \left(\frac{d_5}{d_6}\right) \cos\left(\frac{0.464\pi\lambda_0}{\lambda_g}\right) - \cos(0.464\pi)^2\right)^{-1}} \tag{2.4}$$

$$d_4 = \frac{\lambda_g}{2} \tag{2.5}$$

$$d_5 = \frac{\lambda_c}{2} \tag{2.6}$$

Using Equations (2.2 - 2.6), the nominal dimensions for a WR90 waveguide (operating at 10 GHz) with 4 slots is given in Table 2.1. The waveguide height (d_6) is independent of frequency, but the commonly used nominal height is given. A common metric for measuring antenna performance is the far-field gain of the antenna. Antenna gain is a measure of how well the antenna converts input power into radiated power in a given direction. When the direction is not specified, it refers to the maximum value of the gain. Gain is defined as the ratio between the power radiated in the given direction by the antenna and and a hypothetical lossless isotropic antenna. The gain is often expressed in terms of decibels (dB) as a convenient unit for comparison. The metric used here to compare two antennas will be the maximum far-field antenna gain expressed in dB.

The first step in determining the gain for a waveguide antenna is solving for the electric and magnetic fields in the waveguide's near-field using Maxwell's equations (computed using FEM):

$$\nabla \cdot \mathbf{B} = 0 \tag{2.7}$$

$$\nabla \cdot \mathbf{D} = \rho \tag{2.8}$$

$$\nabla \times \mathbf{H} = \mathbf{J} + \frac{\partial \mathbf{D}}{\partial t} \tag{2.9}$$

$$\nabla \times \mathbf{E} = -\frac{\partial \mathbf{B}}{\partial t} \tag{2.10}$$

where $\mathbf{E}$ is the electric near-field, $\mathbf{M}$ is the magnetic near-field, $\mathbf{D}$ is the electric flux density, $\mathbf{B}$ is the magnetic flux density, $\mathbf{J}$ is the current density, and ρ is the electric charge density. The necessary boundary conditions are:

$$\hat{\mathbf{n}} \times \mathbf{H} = \mathbf{J}_s \tag{2.11}$$

$$\hat{\mathbf{n}} \times \mathbf{E} = 0 \tag{2.12}$$

$$\hat{\mathbf{n}} \cdot \mathbf{B} = 0 \tag{2.13}$$

$$\hat{\mathbf{n}} \cdot \mathbf{D} = \rho_s \tag{2.14}$$

where $\hat{\mathbf{n}}$ is the outward normal vector of the waveguide surface. After solving for the near-field, which is delineated from the far-field by the imaginary surface S, the electric field at some point p in the far-field, $\mathbf{E_p}$, is found using the Stratton-Chu formula [10], which is given as

$$\mathbf{E}_p = \frac{jk}{4\pi}\hat{r}_0 \times \int_S [\hat{n} \times \mathbf{E} - \eta \hat{r}_0 \times (\hat{n} \times \mathbf{H})] \exp(jk\mathbf{r} \cdot \hat{r}_0) dS \tag{2.15}$$

where k is the wave number, $\mathbf{r}$ is the radius vector of the surface S, $\hat{n}$ is the outward unit normal vector of the surface S, $\hat{r}_0$ is the unit vector in the direction of $\mathbf{r}$, and η is the

impedance. The gain at point p is then calculated using the following equation:

$$G_p = 20 \log_{10} \left(\frac{|\mathbf{E}_p|^2}{\sqrt{60 P_{in}}} \right) \tag{2.16}$$

where P_{in} is the power input into the antenna feed. By calculating the gain at a large number of points in a sphere around the antenna, a radiation pattern graph may be produced, which simplifies visualization of the antenna performance. The radiation pattern plots presented here are plotted in a spherical coordinate system, and will use both color and distance from the origin to designate the antenna gain in that direction. An example of a radiation pattern for a four-slot waveguide is shown in Figure 2.3.

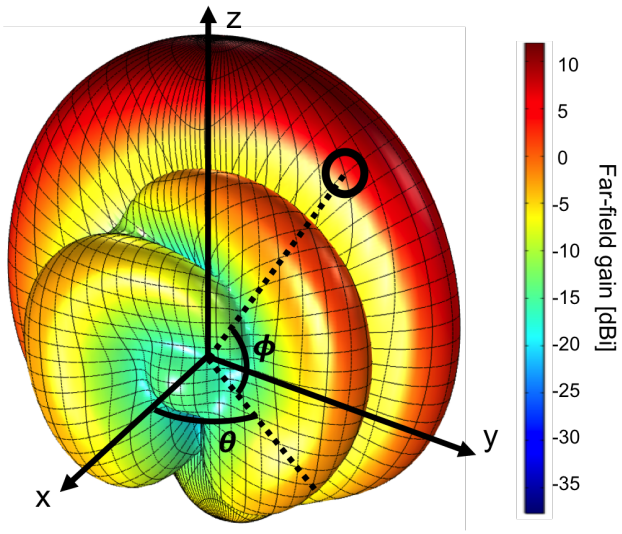

Figure 2.3: Far-field gain pattern of a four-slot waveguide

2.2.2 RF Model for WR90 Slotted Waveguide Antenna

The first step in the multi-fidelity design process is generating an accurate model of the RF radiation pattern of a single waveguide antenna. Ha and Canfield [13] created a high-fidelity FEM model of a WR-90 slotted waveguide antenna for use in a sensitivity study in which the

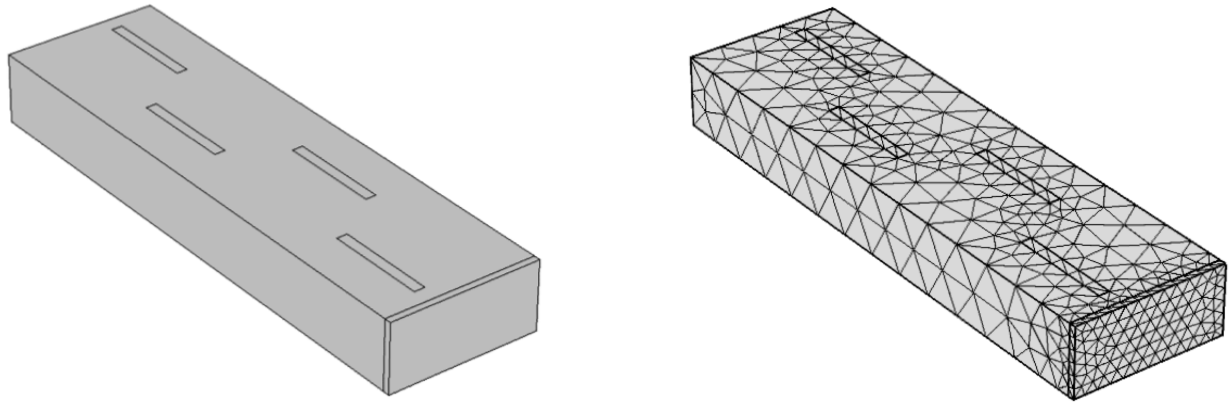

(a) (b)

Figure 2.4: Four-slot waveguide CAD model (a) and its mesh (b)

effects of changing various dimensions of the antenna had on the antenna performance were investigated. This model, shown in Figure 2.4, was generated in COMSOL Multiphysics [9], a commercial computer aided design (CAD) and FEM program.

The model consists of a short four-slot waveguide, with waveguide and slot dimensions as enumerated in Table 2.1.The FEM mesh is a variable-size mesh of two-dimensional triangular shell elements that is automatically generated by COMSOL, using information about the frequency and wavelength to determine element sizes. The waveguide has a thin rectangular port on one end that provides the TE10 electrical feed, and the waveguide is closed on the other end. In order to simulate the antenna radiating into free space without modeling an infinite space, the domain, made up of variable-size tetrahedral elements, is truncated using a perfectly matched layer and a scattering boundary condition to prevent the signal from being reflected at the domain boundary. The waveguide model and simulation domain are shown in Figure 2.5.

Initially, the waveguide material was be set to be a perfect electrical conductor (PEC). This simulates the ideal case, but is not a realistic material property. This ideal PEC will only be used for the initial testing and verification cases, and will be replaced with realistic CFRP

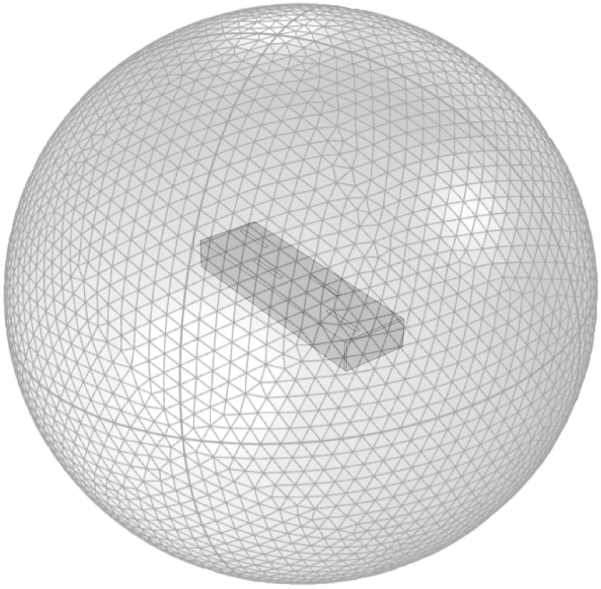

Figure 2.5: Four-slot waveguide shown with simulation domain

material properties. Additionally, for some of the test cases, the model will be expanded to an array of three antenna elements. For the final test case and subsequent optimization, the model is extended from a four-slot waveguide to a 12-slot waveguide.

2.2.3 Array Gain Calculation Using Superposition

Due to the high computational cost of performing FEA on multiple waveguides, it becomes impractical to model arrays of larger than a few elements using such a high-fidelity analysis. However, the fidelity of the FEA cannot be reduced, as the element size would increase beyond the slot size of the waveguide, and would also be unable to capture the effects of such a high frequency field. To solve this problem, a multi-fidelity model is proposed, in which a high-fidelity FEA model is generated for a single waveguide, and the radiation pattern from that waveguide is superimposed upon itself to simulate the radiation from an entire waveguide array. The MATLAB Phased Array Toolbox [17] is used to superimpose

the one-degree resolution data that is exported from the COMSOL FEA results.

To calculate the radiation pattern of a uniformly spaced linear array of N waveguide elements, the total radiation pattern is equal to the radiation pattern for one waveguide element times the array factor AF, which is given as [24]

$$AF = I\frac{\sin\left(\frac{N}{2}(\beta d\cos\theta+\alpha)\right)}{\sin\left(\frac{1}{2}(\beta d\cos\theta+\alpha)\right)} \tag{2.17}$$

where I is the current supplied to the element, β is the phase constant, d is the centerline-to-centerline distance of the waveguides that are placed side by side, θ is the beam steering angle, and α is the inter-element phase shift in the array. These calculations are performed automatically using the MATLAB Phased Array Toolbox for a single four-slot waveguide.

Test Case 1

This test is intended to ensure that there is no loss or alteration of the data, and will consist of a visual inspection of the radiation pattern for significant changes, and comparing the peak gain between the COMSOL and MATLAB models. The model used for this test is the four-slot waveguide model created by Ha and Canfield [13] and adapted with the dimensions given in Table 2.1. This model is shown in Figure 2.6. Once the FEA has been executed and the radiation pattern has been generated, the radiation pattern is exported from COMSOL as a file containing the value of the antenna gain at 129,600 points in the far field, corresponding to a sampling resolution of one degree for all azimuth angles in the range $[0^o, 359^o]$ and elevation angles $[-180^o, 180^o]$. The first test case that will be considered is comparing the radiation pattern in COMSOL to the radiation pattern as rendered from the exported data in the MATLAB Phased Array Toolbox.

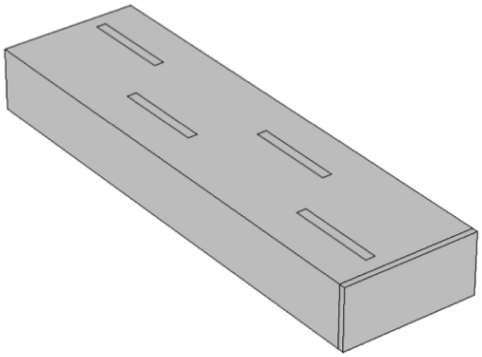

Figure 2.6: COMSOL high-fidelity model of a single waveguide element [8, 13]

Test Case 2

The second test case for verifying the superposition process compares a high-fidelity model of multiple waveguides with a superposition model of the same number of waveguides. Due to the prohibitively high computational cost, the maximum array size able to be modeled with high-fidelity FEA was three waveguides. The FEA model used for Test Case 1 was extended to an array of three waveguides, shown in Figure 2.7. The radiation pattern from this array was compared to a superposition of three antenna elements, the pattern for which was imported to the MATLAB Phased Array Toolbox in the previous test case.

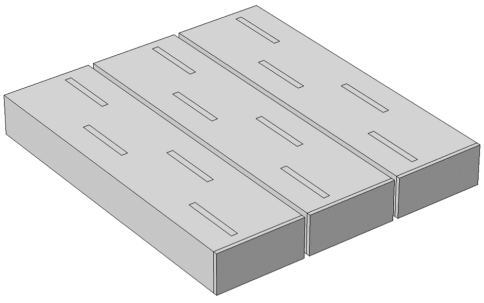

Figure 2.7: COMSOL high-fidelity model of a three-element waveguide array

Test Case 3

For the third test case, to verify the scalability of the superposition process, the array size is increase to nine waveguides, shown in Figure 2.8. Because the computational cost of performing high-fidelity FEA analysis on a nine-antenna array is prohibitively high, a hybrid approach is considered. A superposition of the radiation patterns of three high-fidelity three-waveguide arrays, to create a nine-waveguide array, is compared to a superposition of the radiation pattern of nine individual waveguides.

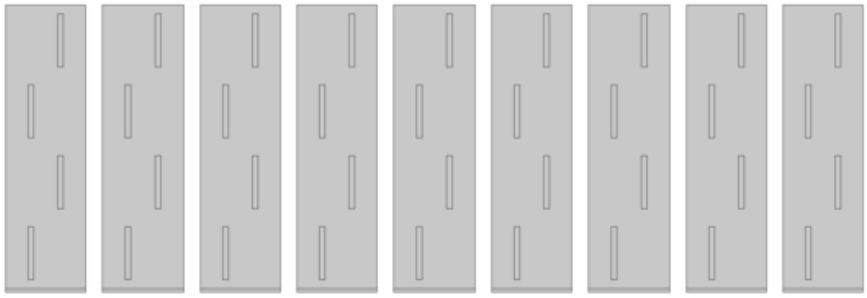

Figure 2.8: Nine-element waveguide array

Test Case 4

The last test case for the process verification is repeating Test Case 1 with a larger waveguide. The four-slot waveguide is useful for quick modeling and verifying the superposition process, but actual SWASS panels will be made with larger waveguides with more slots. The model used for this test, shown in Figure 2.9 is a 30 cm long 12-slot waveguide that was modified from the high-fidelity FEA model from Test Case 1.

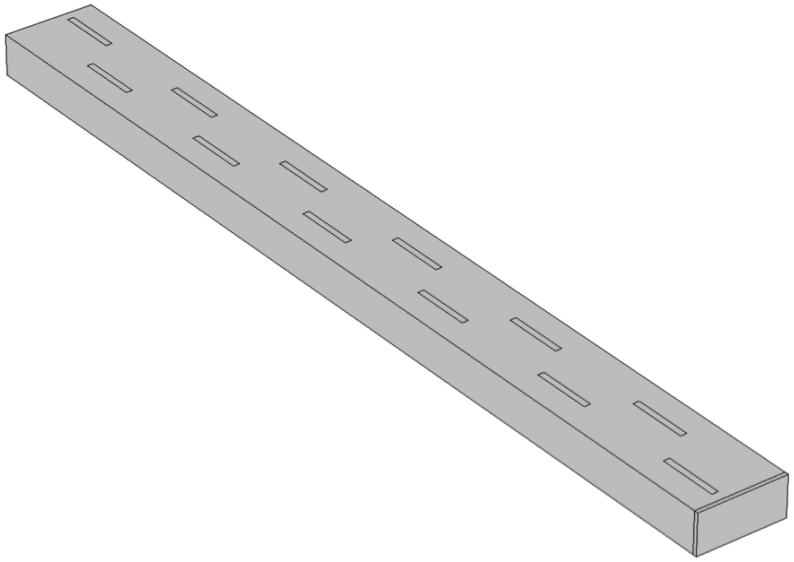

Figure 2.9: COMSOL high-fidelity model of a long waveguide array

2.2.4 Verification With Realistic Material Properties - CFRP

Once the verification process is completed using a perfectly conducting material, the analysis was expanded to more realistic material properties. Callus et al. [7] built and tested a SWASS panel constructed of ten ten-slot waveguide antennas made entirely of carbon fiber reinforced plastic. The component waveguides of the SWASS array were composed of CFRP laminates arranged in a $[0, 90]_S$ stacking sequence, where the 0^o fiber direction is parallel to the longitudinal axis of the waveguide. The electrical properties of CFRP laminates are highly anisotropic, as the conductivity and permittivity are entirely dependent on fiber

direction. Callus et al. give the conductivity tensors σ for CFRP as

$$\sigma 0a = \sigma 0b = \begin{bmatrix} 0 & 0 & 0 \\ 0 & 0 & 0 \\ 0 & 0 & \sigma_L \end{bmatrix} \tag{2.18}$$

$$\sigma 90a = \begin{bmatrix} \sigma_L & 0 & 0 \\ 0 & 0 & 0 \\ 0 & 0 & 0 \end{bmatrix} \tag{2.19}$$

$$\sigma 90b = \begin{bmatrix} 0 & 0 & 0 \\ 0 & \sigma_L & 0 \\ 0 & 0 & 0 \end{bmatrix} \tag{2.20}$$

where 0 and 90 indicate laminates with a 0^o or 90^o fiber orientation, respectively, a indicates laminates located on the broad walls of the waveguide (top and bottom surfaces), b indicates the narrow side of the waveguide, and σ_L has a value of 28,000 S/m. A zero value on the diagonal indicates zero conductivity in that direction, which is normal to the waveguide wall. Here, the z-direction is parallel to the longitudinal axis of the waveguide, the y-direction is normal to the slotted face of the waveguide, and the x-direction is perpendicular to y and z.

Similarly, the permittivity ε tensors are given as

$$\varepsilon 0a = \varepsilon 0b = \begin{bmatrix} \varepsilon_L & 0 & 0 \\ 0 & \varepsilon_L & 0 \\ 0 & 0 & 0 \end{bmatrix} \tag{2.21}$$

$$\varepsilon 90a = \begin{bmatrix} 0 & 0 & 0 \\ 0 & \varepsilon_L & 0 \\ 0 & 0 & \varepsilon_L \end{bmatrix} \tag{2.22}$$

$$\varepsilon 90b = \begin{bmatrix} \varepsilon_L & 0 & 0 \\ 0 & 0 & 0 \\ 0 & 0 & \varepsilon_L \end{bmatrix} \tag{2.23}$$

where ε_L has a value of $30 - 7.4j$. The zero conductivity in the normal direction in Callus's values is an idealization of the CFRP properties, and will be set to a relatively small but non-zero value to ensure a more realistic effective conductivity and to avoid computational errors. The above values are given only for a single laminate, so for a waveguide with a ply stacking sequence of $[0,90]_S$, effective average conductivity and permittivity tensors for the

broad and narrow waveguide walls are created:

$$\sigma_a = \begin{bmatrix} 28000 & 0 & 0 \\ 0 & 1000 & 0 \\ 0 & 0 & 28000 \end{bmatrix} \text{ S/m} \tag{2.24}$$

$$\sigma_b = \begin{bmatrix} 1000 & 0 & 0 \\ 0 & 28000 & 0 \\ 0 & 0 & 28000 \end{bmatrix} \text{ S/m} \tag{2.25}$$

$$\varepsilon_a = \begin{bmatrix} 15 - 3.7j & 0 & 0 \\ 0 & 30 - 7.4j & 0 \\ 0 & 0 & 15 - 3.7j \end{bmatrix} \tag{2.26}$$

$$\varepsilon_b = \begin{bmatrix} 30 - 7.4j & 0 & 0 \\ 0 & 15 - 3.7j & 0 \\ 0 & 0 & 15 - 3.7j \end{bmatrix} \tag{2.27}$$

The peak gain measured for a single waveguide from the SWASS array created by Callus et al. was 12.664 dB, and the peak gain for the ten-waveguide array was measured to be 23.122 dB. The high-fidelity FEA model with 12 slots and perfect electric properties used for Test Case 4 will be modified to have ten slots and the effective CFRP electrical properties shown in Equations (2.24-2.27). The peak gain of this updated model will be compared to that of a single CFRP waveguide from Callus as an experimental validation of the high-fidelity FEA model created by Kim and Canfield and modified here. Additionally, the radiation pattern from the updated model will be superimposed to create a ten-waveguide array, whose gain will be compared to that of the entire SWASS panel from Callus, as further validation of the superposition process.

2.2.5 Waveguide RF Performance Optimization

Traditionally, slotted waveguide antennas are built according to the nominal dimensions established decades ago using Elliott's analytical analysis [11]. As Elliott's method is general for waveguides of all frequencies, and a high-fidelity validation of Elliott's values has not been performed, the established dimensions may turn out to not be optimal for this application. Additionally, two future goals of this project are to analyze the structural strength of SWASS panels and to find an optimal design that balances strength with RF performance. Ha et al. [13] performed a sensitivity study to determine which of the waveguide dimensions had the greatest effect on the electrical performance and which could be altered slightly in favor of increasing the waveguide strength. In their sensitivity analysis, Ha et al. determined that the EM performance of a waveguide has low sensitivity to three of the design variables: slot width, longitudinal slot spacing, and waveguide height. It is likely that these low-sensitivity variables will be critical for optimizing the structural strength of the waveguide without compromising the EM performance. The design variables with very high sensitivity were determined to be slot length, slot spacing from the centerline, and waveguide width. These dimensions greatly affect the maximum antenna gain, so it is likely that these variables will not be permitted to change significantly. In the next section, a single-objective optimization is performed to determine the set of the waveguide dimensions that will result in the maximum peak gain of a 12-slotted waveguide antenna. This optimum design for RF performance will later be used as the utopia point for the RF objective in the multi-objective design.

Coarse Optimization Proof of Concept

Before spending the computational power to perform a high-fidelity optimization of the electromagnetic performance of the 12-slot waveguide, a preliminary coarse optimization

was completed using the small four-slot waveguide model, as used in Test Case 1. Due to the complexity of the model, the objective and its gradient cannot be calculated analytically, so gradient-based optimization methods are not applicable and a non-gradient-based method must be utilized. As determined by Ha et al. [13], the maximum far-field gain of a slotted waveguide antenna is highly sensitive to some of the design variables. The genetic algorithm was chosen over other gradient-free methods because the level of randomness inherent to the method is necessary to ensure that the solver does not get caught in a local minimum.

The genetic algorithm is a non-gradient based optimization method that was inspired by biological evolutionary processes. A starting "population" of candidate solutions, also known as individuals, is randomly generated. Then, the fitness of each individual is evaluated according to the objective function. If an individual scores well, it is selected to "reproduce" with another member of the population, and through a process similar to biological reproduction, a new individual is created using a random selection of its parents' properties. Thus, a new generation of potential solutions is created. As with biological evolution, random mutation of the individuals may occur from generation to generation. In this manner, better solutions are preferentially selected, and with enough iterations, the genetic algorithm may arrive at the optimum solution.

This optimization was implemented using the genetic algorithm contained within MATLAB's Global Optimization Toolbox [18] The MALTAB genetic algorithm requires function evaluations to be made using a MATLAB script. COMSOL comes equipped with the ability to communicate with MATLAB in the command line by providing a suite of MATLAB functions that allow parameters in the FEA model to be modified, simulations to be run, and function values to be returned to MATLAB. Using these functions, a MATLAB function was produced to interface with COMSOL in order to provide the model dimensions, run the FEM simulation, and return the peak far-field gain value for each population member.

Each generation consisted of twenty population members. The population size was chosen to be small because of the extensive time required for function evaluations. The initial population consisted of twenty randomly generated members whose design variables are within 10% of the nominal values from Wade [26]. With such a small population, only one member of each generation is guaranteed to survive to the next generation, while fifteen members are produced using crossover. A Gaussian mutation function was used for determining the new populations. The solver was run until the average relative change in the best fitness function value over fifty generations is less than or equal to 10^{-6} dB, to ensure that the optimizer did not get stuck in a local minimum.

The objective function to be evaluated is the maximum far-field gain. Several constraints on the design variables are necessary to prevent geometries that are physically impossible (such as overlapping slots or slots extending beyond the outer waveguide dimensions). The constraints used are:

$$d_1 + 2d_3 - d_5 < 0 \tag{2.28}$$

$$2d_1 - d_5 < 0 \tag{2.29}$$

$$d_2 - 2d_4 < 0 \tag{2.30}$$

$$d_1 - 2d_3 < 0 \tag{2.31}$$

$$d_2 + 3d_4 < L \tag{2.32}$$

High-Fidelity Optimization

The results from the genetic algorithm optimization of the small four-slot waveguide are given in Section 2.3.3. The results show that the analytically approximated nominal values given by Wade [26] may not be optimal for all waveguide configurations, and the maximum

far-field gain of a slotted waveguide may be improved with high-fidelity optimization. For a SWASS panel to achieve the maximum far-field gain, it follows that the individual waveguides within the panel must be optimized to produce the maximum far-field gain. The waveguides that was used in the final SWASS panel for the X-47 case study are 30 cm in length with 12 slots, as in Test Case 4, and will have the electrical properties outlined in Section 2.2.4.

The optimization of the 12-slot waveguide with realistic CFRP electrical properties will be performed using the Nelder-Mead optimization method, another non-gradient based method. This method differs from the genetic algorithm in that it searches through the design space in a more systematic manner, rather than the mostly random search of the genetic algorithm. In an n-dimensional design space, the algorithm works by forming a "simplex", a geometric object with n+1 flat sides. The local behavior near the vertices of the simplex is evaluated, and a new simplex is formed by replacing the vertex with the lowest objective function value with a new one, that ideally would have a better function value.

The objective function to be maximized is the same as in the previous section: the maximum far-field gain. The same constraints were applied to this optimization, with some additional side constraints to further ensure that errors do not occur during the optimization:

$$0.001 \text{ m} \leq d_1 \leq 0.003 \text{ m} \tag{2.33}$$

$$0.008 \text{ m} \leq d_2 \leq 0.016 \text{ m} \tag{2.34}$$

$$0.002 \text{ m} \leq d_3 \leq 0.007 \text{ m} \tag{2.35}$$

$$0.017 \text{ m} \leq d_4 \leq 0.021 \text{ m} \tag{2.36}$$

$$0.018 \text{ m} \leq d_5 \leq 0.027 \text{ m} \tag{2.37}$$

$$0.008 \text{ m} \leq d_6 \leq 0.012 \text{ m} \tag{2.38}$$

An additional constraint was added to prevent the mass of the waveguide from exceeding that of the waveguide with nominal dimensions, to preserve the weight-saving goal of the dual-purpose structure. This constraint will also be important when the structural strength is considered later, since a structural optimization without this weight constraint would use as much material as possible to increase the buckling load of the waveguide.

2.2.6 SWASS Panel Evaluation

Once the 12-slot CFRP waveguide is optimized for maximum far-field gain, the performance of the entire X-47 SWASS panel can be evaluated. The RF performance of the SWASS panel will be determined using the same superposition process outlined in Section 2.2.3, in which the radiation pattern of the single waveguide is generated in COMSOL and superimposed using the MATLAB Phased Array Toolbox. The performance of this full SWASS panel can then be compared to commercially available weather radar antennas, and the suitability for use on the X-47 unmanned aircraft can be evaluated.

2.3 Results

2.3.1 Superposition Verification

Test Case 1

The first verification test required was ensuring that there is no loss of data as a model is imported from COMSOL into the MATLAB Phased Array Toolbox. The far-field gain pattern from the high-fidelity FEM generated in COMSOL is shown below in Figures 2.10a and 2.10b. The response data from this simulation was imported into MATLAB and plotted

using the Phased Array Toolbox, and is shown in Figures 2.10c and 2.10d for comparison. It is evident that there is negligible change in the radiation pattern when the model is imported to MATLAB. The peak far-field gain for this antenna is 12.6 dB, and the same peak gain is reflected in the imported model.

Test Case 2

Using the same high-fidelity model, an antenna array of three side-by-side elements was created. The far-field gain pattern of this array was calculated in COMSOL using high-fidelity FEM and imported to MATLAB, shown below in Figure 2.11a. The peak far-field gain for this array is 17.1 dB. This array was compared to an identical array created in MATLAB, built from the same MATLAB model in Test Case 1. The far-field gain pattern of this array was calculated in the MATLAB Phased Array Toolbox, using only superposition calculations. This radiation pattern is shown in Figure 2.11b. The peak far-field gain for this array is 18.4 dB. Upon inspection, it is evident that the patterns have significant qualitative differences, most likely due to the fact that MATLAB is not able to take mutual interference effects into account. As the most mission-critical metrics for analyzing antenna performance, the main (boresight) and side lobe peak levels were compared to provide a quantitative method of comparison. The relative error between the peak gain values for the two antenna arrays and the angular error between the lobe pointing directions for several lobes are shown in Table 2.2.

Table 2.2: Test Case 2 Peak Gain Error

	Gain Relative Error	Angular Error
Boresight Lobe	2.36%	0°
Main Side Lobe	10.42%	5.36°
Minor Side Lobe	0.35%	1.41°

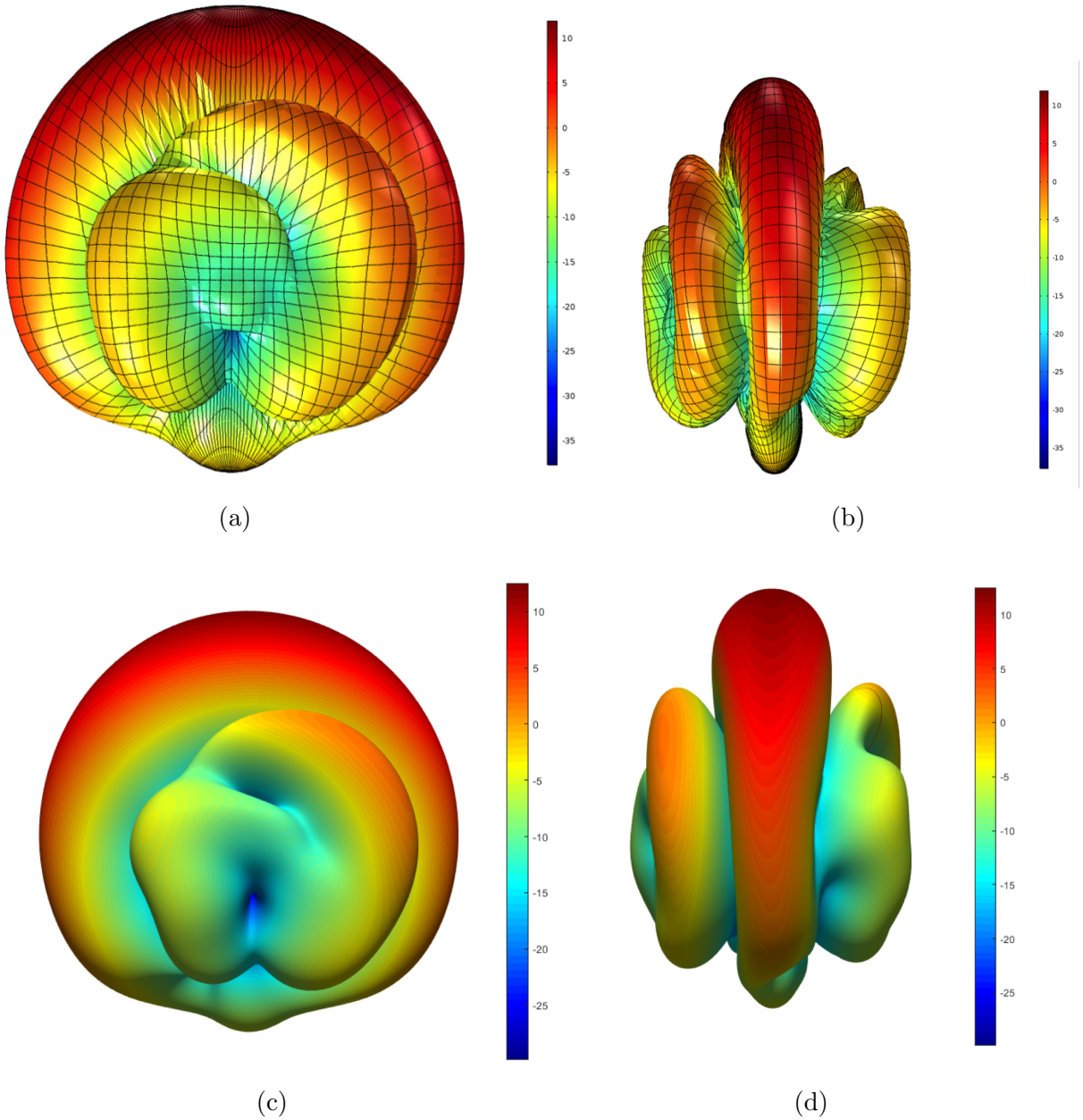

Figure 2.10: Single waveguide far-field gain (dB). COMSOL high-fidelity (a) front and (b) side views. (c) Front and (d) side views after importing to MATLAB.

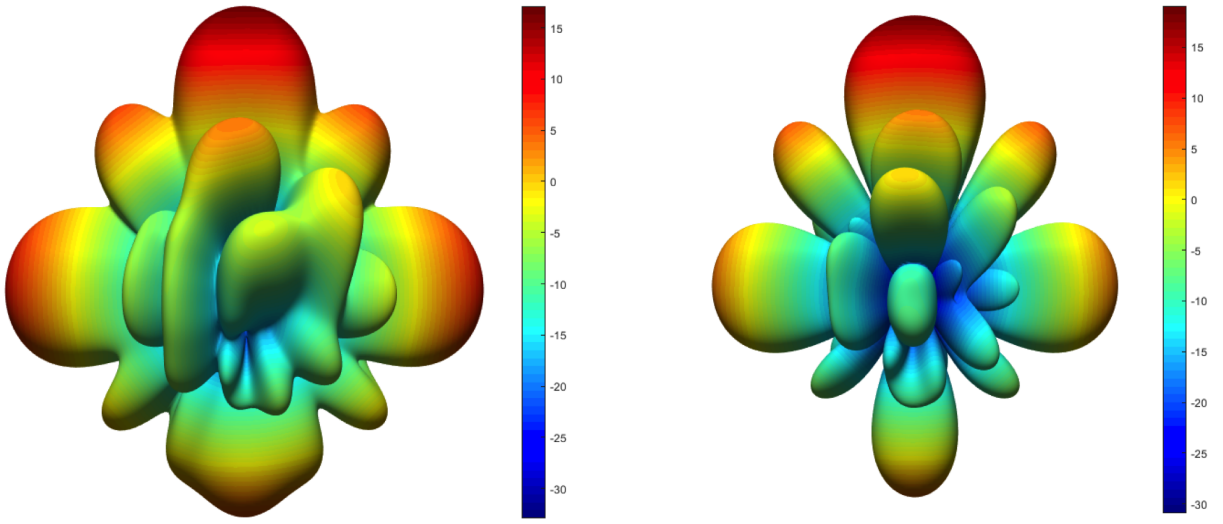

(a) (b)

Figure 2.11: Three waveguide array far-field gain (dB). (a) COMSOL high-fidelity and (b) MATLAB superposition

Test Case 3

For the third test case, three copies of the three-element FEM model were superimposed to create a larger linear array consisting of nine waveguide elements. The far-field gain pattern, as calculated in the MATLAB Phased Array Toolbox, is shown in Figure 2.12a. The peak far-field gain for this array is 22.4 dB. This gain pattern was compared to that of another linear array, made up of nine copies of the single-element FEM model, similarly calculated using the Phased Array Toolbox. The gain pattern for this array is shown in Figure 2.12b. The peak far-field gain for this antenna is 23.5 dB. The same method for quantitatively comparing two far-field gain patterns used for Test Case 2 was implemented for this test case. These results are shown in Table 2.3.

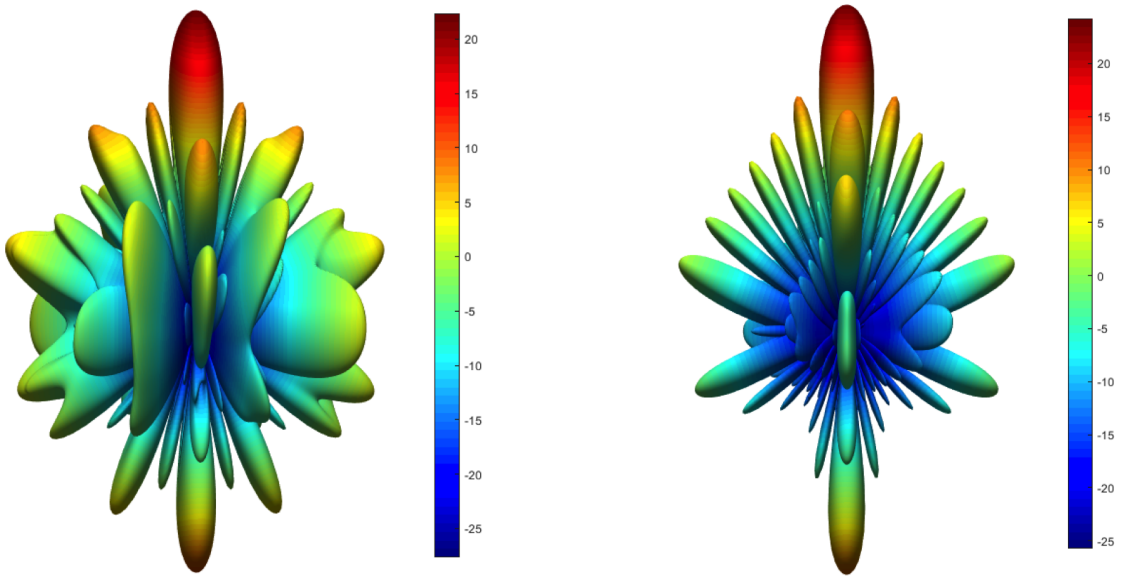

(a) (b)

Figure 2.12: 9-Waveguide array far-field gain (dB). (a) Superposition of three 1x3 arrays and (b) superposition of 9 single elements.

Table 2.3: Test Case 3 Peak Gain Error

	Gain Relative Error	Angular Error
Boresight Lobe	1.15%	0º
Main Side Lobe	6.66%	1.00º
First Minor Side Lobe	1.93%	1.00º
First Front Lobe	1.03%	2.00º
Second Front Lobe	0.34%	1.00º

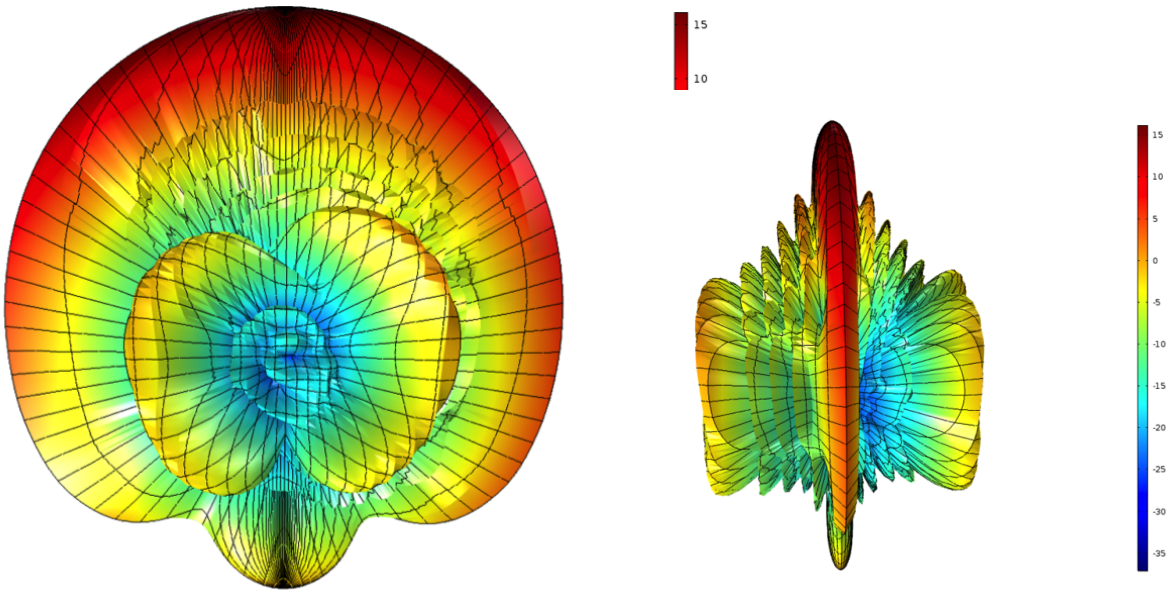

(a) (b)

Figure 2.13: Single long 12-slot waveguide far-field gain (dB). COMSOL high-fidelity (a) front and (b) side views.

Test Case 4

In order to model an antenna array of the size that could potentially be used as a weather radar system on the X-47 unmanned aircraft, it was necessary to create a larger waveguide element to be superimposed. The far-field gain pattern of this antenna is given in Figures 2.13a and 2.13b.

The resulting far-field gain pattern is qualitatively similar to that of the shorter waveguide. The increased number of ridges in the pattern is due to the greater number of slots in the longer waveguide, as the slots are where the electrical field is radiated. Additionally, this antenna has a greater maximum gain, 16.2 dB, indicating that it is more than twice as efficient at radiating the input power compared to the shorter waveguide, which had a maximum gain of only 12.6 dB.

Observations

Test Cases 1 and 4 revealed that there is negligible change in information exported from the high-fidelity model in COMSOL to the superposition model in the MATLAB Phased Array Toolbox. Although the far-field gain patterns for antenna arrays created using FEM and superposition appear to have significant qualitative differences, the mission-critical measures of antenna performance had relatively low error. The main side lobe is the largest source of error in all cases, but this error decreased as the size of the array increased. For the nine-element arrays, there was less than 2% peak relative error for the test locations other than the main side lobe, and even the main side lobe peak error was less than 7%. Additionally, there was very low angular error at all test locations for the nine-element arrays (2^o or less). Since the superposition calculations do not produce relative peak error of greater than 2% for the main lobe or 10% for the side lobes, or angular error of greater than 5^o for the nine-element array test case, it is concluded that superposition of high-fidelity FEM models is a feasible method for modeling larger waveguide antenna arrays.

2.3.2 CFRP Material Properties Verification

The waveguide model used in Test Case 4 was modified to have a total of ten slots and the PEC material properties to changed to those of CFRP given by Callus et al. The peak far-field gain of this model was found to be 12.671 dB, compared to the 12.664 dB as found by Callus et al., which is a difference of just 0.007 dB. When this model was superimposed to create a ten-waveguide array using the Phased Array Toolbox, the peak far-field gain was found to be 27.907 db, as compared to the 23.122 dB as found by Callus et al., a difference of 4.785 dB. The model used by Callus et al. includes the additional models of the power supplies and backshorts, as well as the mutual interference between waveguides,

which accounts for this difference.

2.3.3 Waveguide EM Optimization

Coarse Optimization - Genetic Algorithm

A coarse genetic algorithm optimization was performed using a short four-slot waveguide with PEC material properties as a proof-of-concept to determine if the approximated nominal values developed by Elliott could be improved. The genetic algorithm converged to a solution after 132 generations to a peak far-field gain value of 12.918 dB. The solver terminated because the relative error in the best value of each generation for fifty generations remained below the termination criterion of 10^{-6} dB. For comparison, the nominal dimensions result in a peak far-field gain value of 12.578 dB, which is a difference of 0.340 dB. The convergence history for the optimization is shown in Figure 2.14. In this plot, the "Best fitness" is the member of the population that had the highest peak far-field gain, and the "Mean fitness" shows the average peak far-field gain of that generation's population. The waveguide dimensions that result in the optimum peak far-field gain are shown alongside the nominal dimensions in Table 2.4. A geometric comparison of the nominal and optimal waveguide models is shown in Figure 2.15. It is clear that the slot size and position changed significantly from the nominal configuration to the optimum. The far-field gain patterns for the nominal and optimal waveguides are shown in Figure 2.16. It is difficult to see a significant difference here, as the colorbars have slightly different scales, but there are some minor changes in the shape of the field and the coloring in some areas. However, the measurable increase in peak far-field gain indicates that the nominal values approximated using Elliott's equations are not optimal for all situations, so a higher-fidelity optimization is justified.

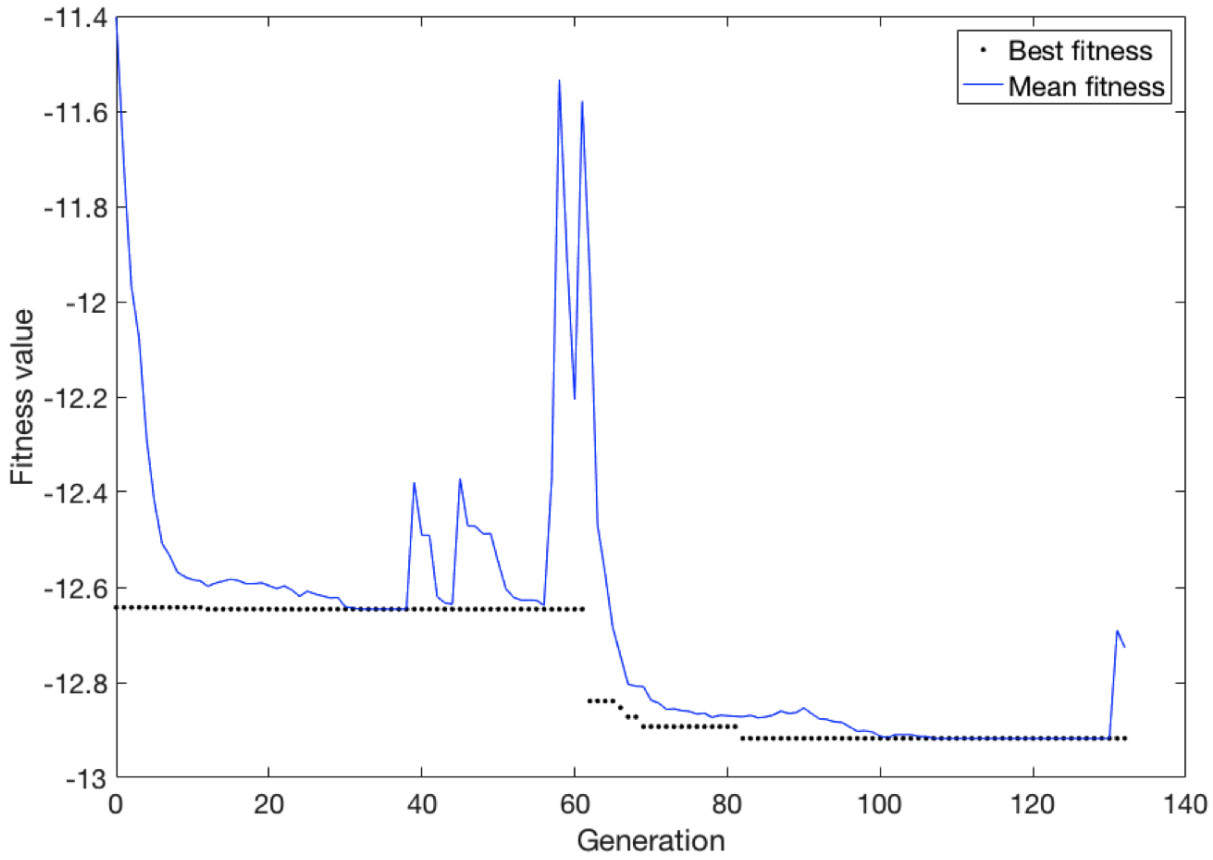

Figure 2.14: Genetic Algorithm Convergence Plot

High-Fidelity Optimization - Nelder-Mead

Because the coarse proof-of-concept optimization and CFRP material implementation were successful, a higher-fidelity optimization was performed using the long 12-slot waveguide used in Test Case 4 with CFRP material properties. The Nelder-Mead method was chosen for this optimization because it performs a more systematic search of the design space. The Nelder-Mead optimization of the 12-slot waveguide with CFRP material properties converged to a solution after 82 iterations to a peak far-field gain of 14.049 dB. This is an extremely significant improvement of 4.396 dB over the waveguide with nominal dimensions, that had a peak gain of 9.653 dB. The convergence history for the optimization is shown in Figure

Table 2.4: Coarse EM Optimization - Optimum Waveguide Dimensions

Variable	Description	Nominal Value	Optimum Value	% Difference
d_1	Slot width	1.59 mm	2.928 mm	84.2%
d_2	Slot length	14.55 mm	14.164 mm	2.7%
d_3	Slot offset from centerline	2.14 mm	4.525 mm	114.5%
d_4	Longitudinal slot spacing	19.88 mm	20.532 mm	3.3%
d_5	Waveguide width	22.86 mm	23.109 mm	1.1%
d_6	Waveguide height	10.16 mm	10.256 mm	0.9%

Table 2.5: High-Fidelity EM Optimization - Optimum Waveguide Dimensions

Variable	Description	Nominal Value	Optimum Value	% Difference
d_1	Slot width	1.59 mm	2.993 mm	+88.2%
d_2	Slot length	14.84 mm	13.255 mm	−10.7%
d_3	Slot offset from centerline	4.22 mm	2.593 mm	−38.6%
d_4	Longitudinal slot spacing	19.88 mm	19.539 mm	−1.7%
d_5	Waveguide width	22.86 mm	20.704 mm	−9.4%
d_6	Waveguide height	10.16 mm	11.021 mm	+8.5%

2.17. The waveguide dimensions that result in the optimum peak far-field gain are shown alongside the nominal dimensions in Table 2.5. A geometric comparison of the nominal and optimal waveguide models is shown in Figure 2.18. For this optimization, none of the constraints are active. This is not unexpected, as the constraints used were not behavioral constraints.

2.3.4 Large Array Modeling

An antenna array consisting of 40 WR-90 slotted waveguide antennas arranged linearly side by side forms a panel of approximately 1 m × 0.3 m. A panel of this size could easily replace one of the panels on the wing of an X-47 aircraft, to be used as a weather radar system. For this application, the antenna array would be configured as an end-fire array, meaning that the EM field is electrically steered, by phasing the input signals, such that the main

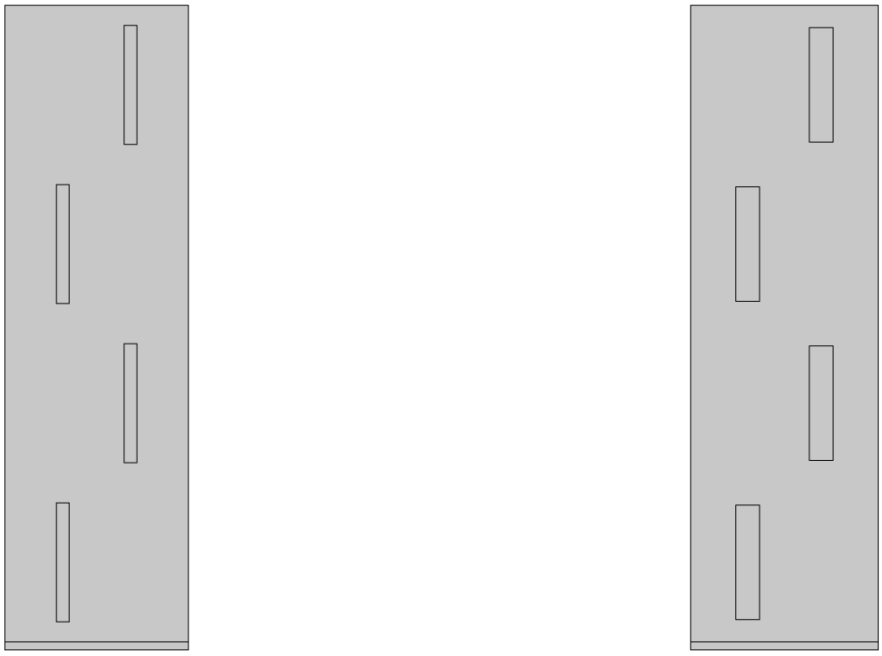

(a) (b)

Figure 2.15: Waveguide geometric configurations (a) before and (b) after genetic algorithm optimization

beam (boresight) direction is along the length of the waveguide. A waveguide antenna array could potentially be placed in the leading edge of a wing, using shorter waveguides, and be configured for broadside firing (normal to the slotted surface).However, in this configuration the leading edge of the wing would need to be electrically transparent (like a radome) and the array may not bear any loads. The optimized waveguide model developed in the previous section was imported to the Phased Array Toolbox for superposition in a 40-element array.

The side view of the far-field gain pattern (Figure 2.20d) shows a great number of side lobes on each side of the main beam. These side lobes correspond roughly to one side lobe per waveguide, so there should be approximately 40 side lobes on each side. Additionally, the side view in Figure 2.20c shows more side lobes than the side view of the gain pattern for the nine element array (Figure 2.12b), which corresponds to the increased number of slots in

each waveguide. As the number of waveguides in a panel increases, the main lobe (and peak gain) increases in strength while the side lobes increase in number but decrease in strength. The array panel has a maximum far-field gain of 35.0 dB. This is a peak gain of almost 21 dB over that of a single 30 cm waveguide element.

2.4 Conclusion and Future Work

A computationally low-cost method for modeling large waveguide arrays was developed using multi-fidelity modeling. Calculating the far-field gain of a waveguide using FEM requires meshing the entire sphere of space around the waveguide, in addition to meshing the waveguide itself. This means that as waveguide length or number of waveguides increases, the number of degrees of freedom in the FEM calculation grows cubically. This prohibits modeling larger arrays without using distributed computing or other types of supercomputers, so superposition, which is much less computationally expensive, may be used to model large arrays. Using several test cases, this process was verified to have low peak far-field gain error, side lobe far-field gain error, and lobe angular error.

To provide a more realistic model, the perfect electrical properties were changed to be real values for CFRP material. The implementation of these material properties was validated and the superposition process was again verified against CFRP waveguide values determined experimentally. The peak far-field gain from the single waveguide matched almost perfectly with the literature value. However, the array peak gain was off by a few decibels, which may be due to the fact that the power supply, backshort, and mutual interference are modeled in the literature and are not modeled here.

A coarse genetic algorithm optimization was performed on a short four-slot waveguide as a proof-of-concept step to see if the peak far-field gain could be improved by modifying

Elliott's values. A modest improvement was seen, so the full-scale high-fidelity optimization was performed using the Nelder-Mead method on a larger 12-slot waveguide with realistic CFRP electrical properties. This optimization resulted in a peak far-field gain of 14.05 dB, an improvement of 4.40 dB over the nominal configuration gain of 9.65 dB.

This optimized waveguide far-field gain pattern was then used in the validated superposition method to create an electromagnetic model of approximately the same size as a wing panel on a Northrop-Grumman X-47 unmanned aircraft. This panel consisted of 40 WR-90 waveguide elements of length 30 cm, resulting in a panel with dimensions of 1 m by 0.3 m. The peak far-field gain of this panel was found to be 34.92 dB, 2.18 dB greater than that of an array of the same size with waveguides of nominal dimensions, which was 32.74 dB. A difference of 2.18 dB seems small at first glance, but given that decibels are on a log scale, the optimized SWASS panel has a peak far-field gain of more than 65% greater than that of the nominally dimensioned SWASS panel.

Now that an electromagnetic model of the full-size panel has been developed, its performance as a weather radar system will be compared to more conventional systems. Further work will focus on modeling the structural performance of SWASS arrays to further contribute to an airworthiness certification process for their use in aircraft. Further research will include the dual-faceted design optimization of the EM performance and structural strength of SWASS arrays. As work continues on this project, the airworthiness certification process will require higher fidelity models that include more components in the models, such as power supplies and backshorts, and an accurate depiction of the mutual interference effects between the waveguides within a SWASS array.

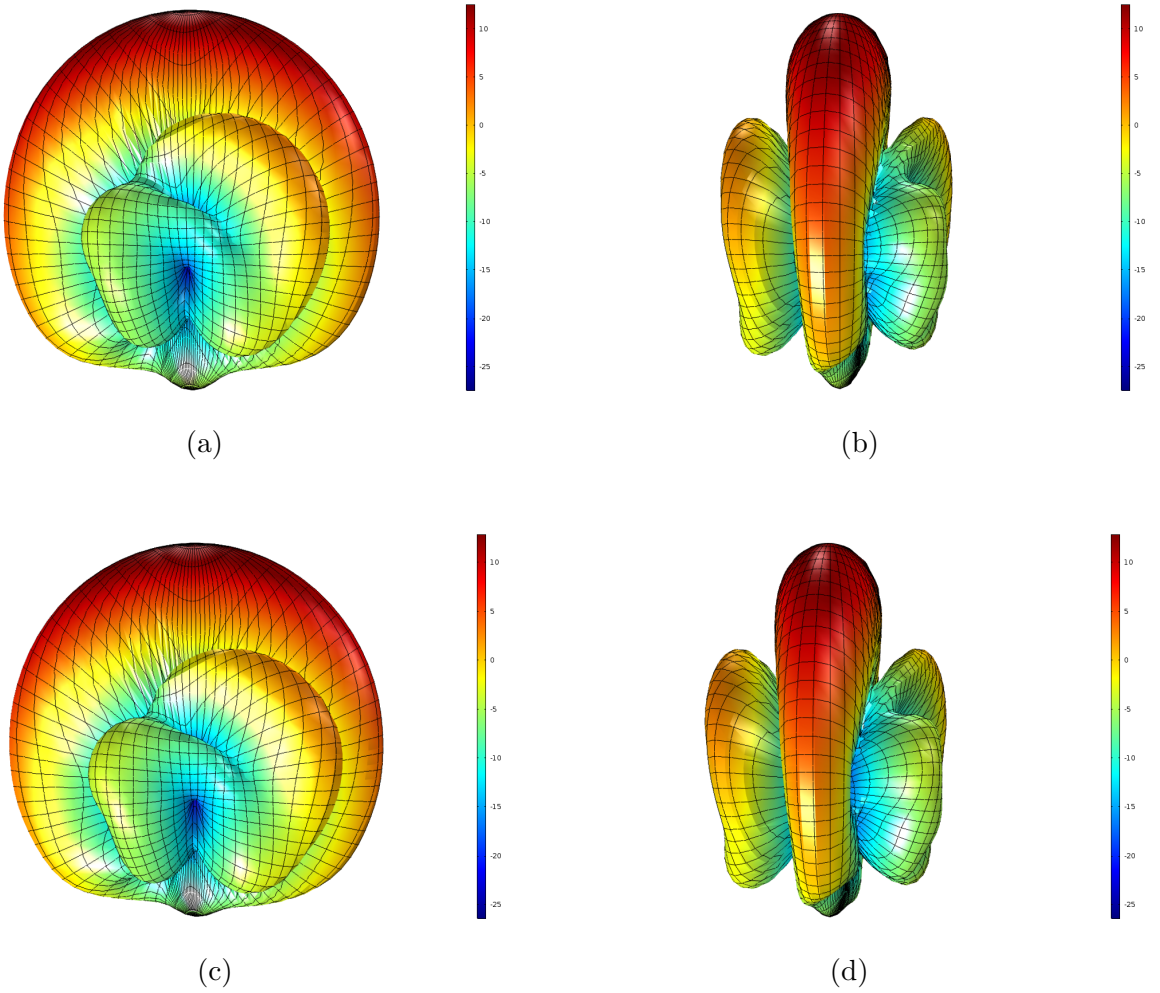

(a) (b)

(c) (d)

Figure 2.16: Far-field gain patterns before and after coarse genetic algorithm optimization. Waveguide with nominal dimensions (a) front and (b) side views. Waveguide with EM-optimized dimensions (c) front and (d) side views.

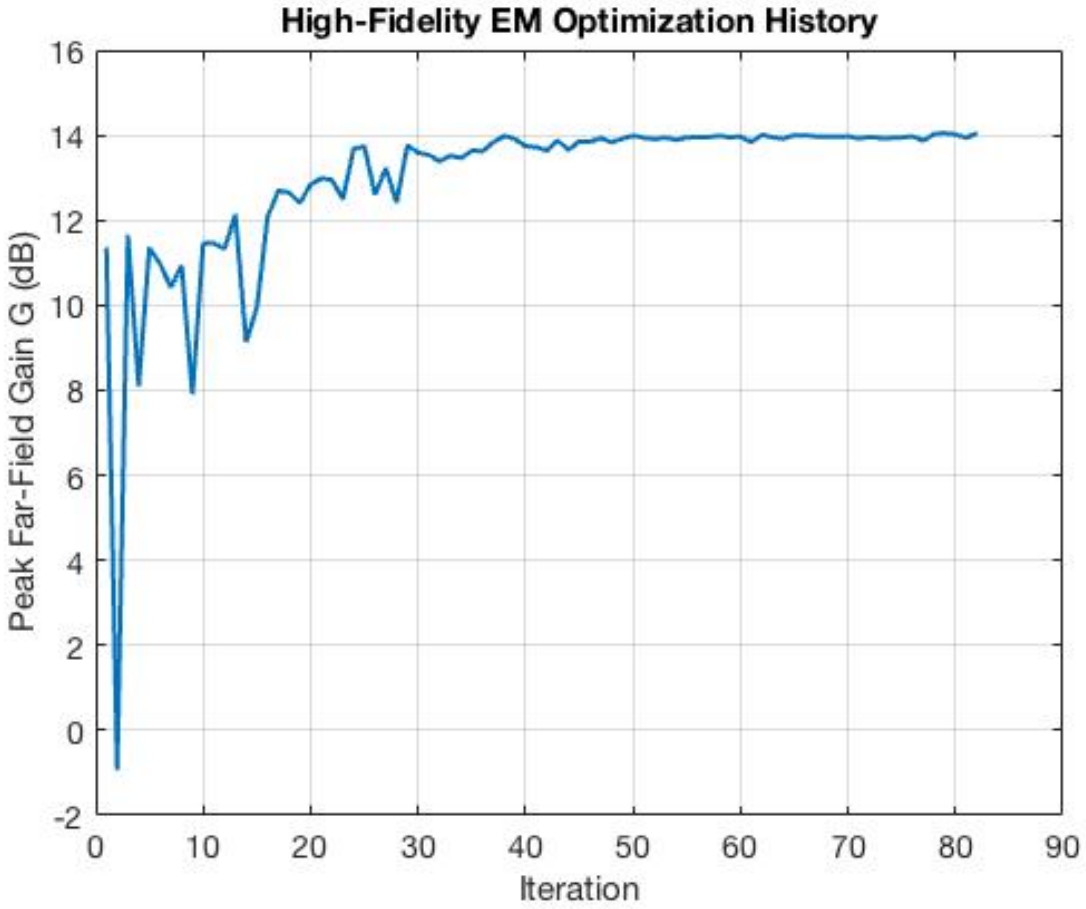

Figure 2.17: Nelder-Mead Convergence Plot

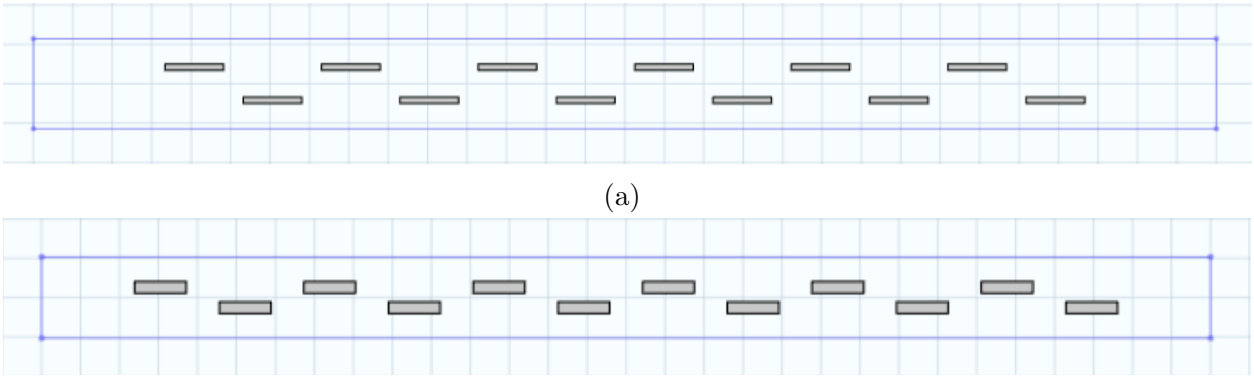

(a)

(b)

Figure 2.18: Waveguide geometric configurations (a) before and (b) after Nelder-Mead optimization

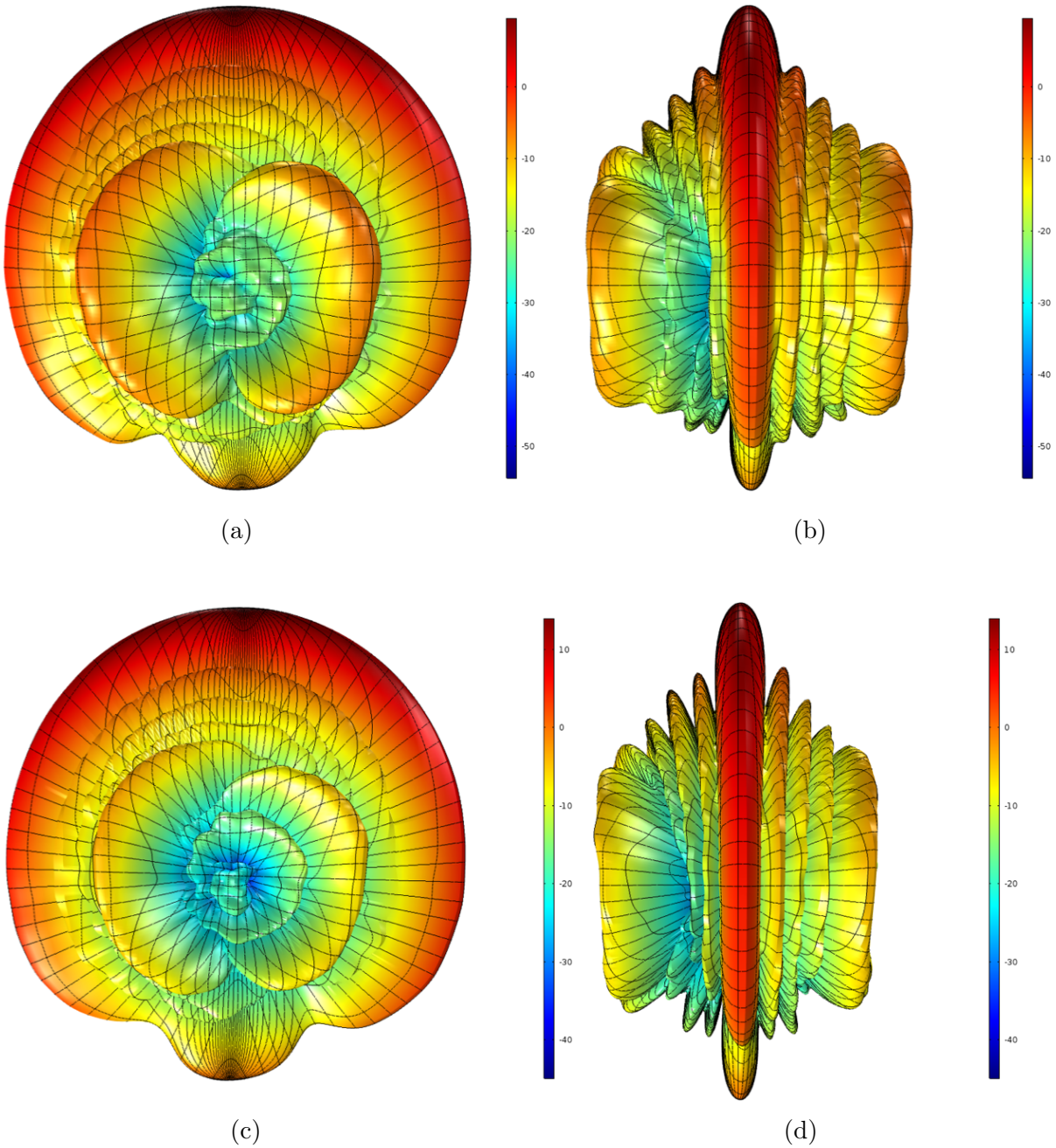

Figure 2.19: Far-field gain patterns before and after high-fidelity Nelder-Mead optimization. Waveguide with nominal dimensions (a) front and (b) side views. Waveguide with optimized dimensions (c) front and (d) side views.

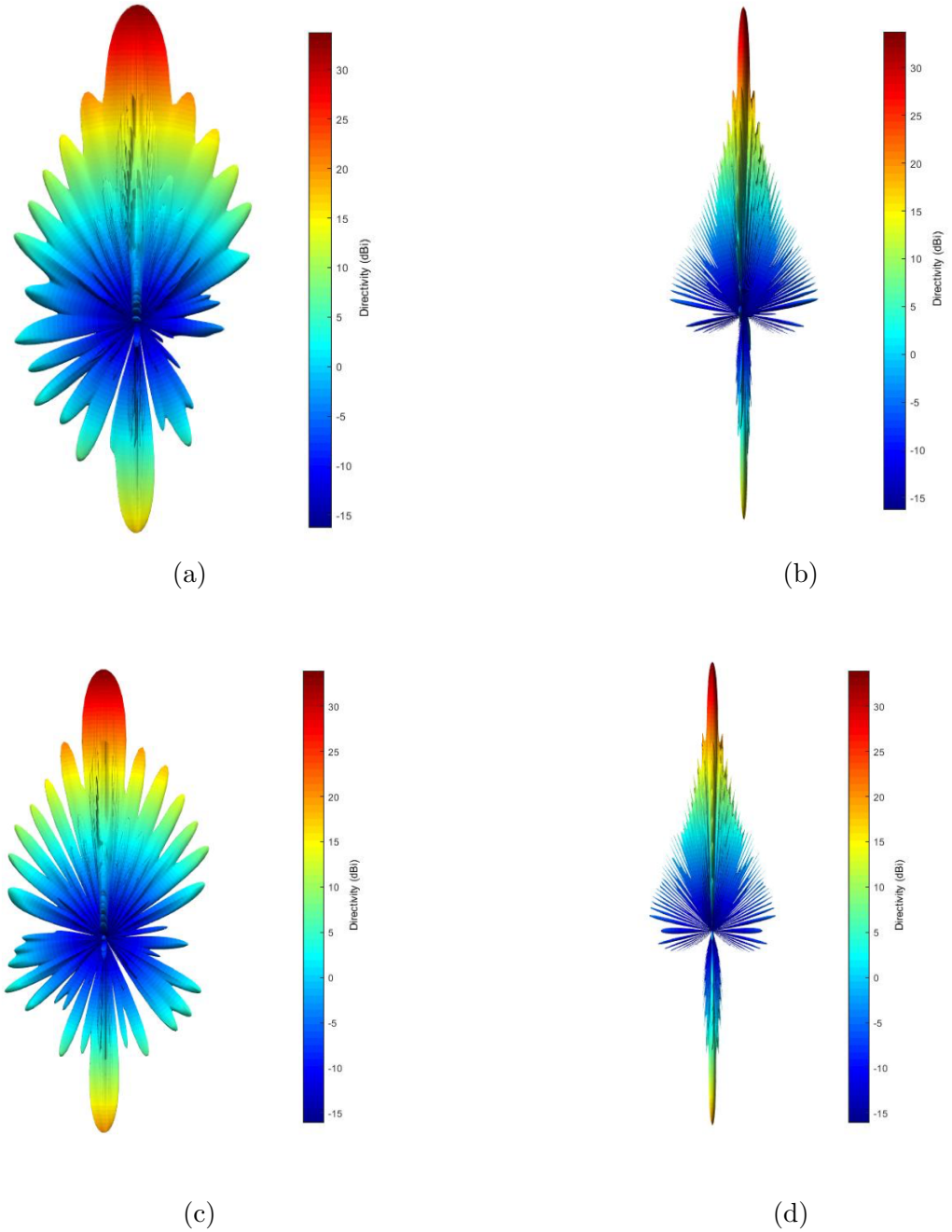

(a) (b)

(c) (d)

Figure 2.20: 40-waveguide SWASS array far-field gain patterns before and after high-fidelity EM optimization. Array consisting of waveguides with nominal dimensions (a) front and (b) side views. Array of dual-optimized waveguides (c) front and (d) side views.

Chapter 3

Structural Design Methods for SWASS

The remainder of this thesis will focus on the research goal of determining the set of waveguide dimensions that balance the electrical performance and load-bearing requirements of SWASS. Without minimum weight and slot size constraints, the structural optimization would send the slot size to zero, as the greater amount of material and lack of stress concentrations would increase the structural strength. However, the electromagnetic performance is highly dependent on slot size, which is a function of the wavelength. Therefore, the optimum dimensions for total SWASS panel performance is neither the optimum EM dimensions nor optimum structural dimensions. To determine this overall optimum, a multi-objective optimization must be performed.

3.1 Waveguide Structural Performance Optimization

3.1.1 Coarse Optimization Proof of Concept

In Chapter 2, before a high-fidelity optimization of the waveguide EM performance was performed, a coarse, low-cost optimization was first performed to determine if some improvement in EM capabilities could be attained over the nominal dimensions, before moving on to a higher-fidelity optimization. This process will be repeated here for the structural optimization.

While SWASS panels could theoretically replace almost any skin panel on an aircraft, the case study used here is of a SWASS panel embedded in the wing of the X-47 aircraft, as shown in Figure 2.1. The aerodynamic loading on the wing would cause the SWASS panel in this configuration, and therefore its component waveguides, to experience compression in the lengthwise direction. As the waveguides can be considered to be slender structures, and the slots cause stress concentrations, two failure modes must be considered: yielding and buckling. The goal of this optimization is to maximize the critical buckling load, while also ensuring that the stresses developed in the top surface of the waveguide will not cause yielding.

The waveguide to be considered is a modified WR-90 waveguide with 12 slots, intended for operation at 10 GHz for weather radar. For buckling, the waveguide will be modeled as a hollow rectangular tube with a smeared effect of the slots for the top surface. Kim et al. [15] used a similar smearing of slots, but smeared the effect of the whole tube to arrive at an equivalent moment of inertia. This smearing of the whole waveguide led to significant error compared to the analytical results, but the trends were still visible. The equivalent moment of inertia calculation used here is smearing much less of the waveguide, so it should result in

Table 3.1: Material properties of copper

σ	Yield stress	70 MPa
$\overline{E}$	Young's modulus	119 GPa
ρ	Density	8960 kg/m^3

substantially less error. The critical buckling load P_{cr} will be calculated using Euler column buckling formula for a pinned-pinned member:

$$P_{cr} = \frac{\pi^2 \overline{EI}}{L^2} \tag{3.1}$$

where $\overline{E}$ is the Young's modulus of the material, $\overline{I}$ is the waveguide cross-sectional moment of inertia, and L is the waveguide length. For yielding in the slotted surface, Finite Element Analysis (FEA) of the top face of the waveguide will be performed using two-dimensional membrane elements. For this preliminary analysis, the material properties of copper will be used as a benchmark, and are listed in Table 3.1.

To simplify the buckling analysis, the effects of the slots are smeared by using a hollow rectangular tube with no holes, where the upper face thickness is taken to be constant across the entire waveguide and has an equivalent amount of material as the real upper face, as shown in Figure 3.1. The equivalent upper face thickness t_u is:

$$t_u = t\left(1 - \frac{N d_1 d_2}{(W - 2t)L}\right) \tag{3.2}$$

The cross-section is divided into four sections, also shown in Figure 3.1, which are used for calculating the moment of inertia. After taking the new upper face thickness into account, the neutral axis y will change slightly from its original value of H/2, and must be recalculated:

$$y = \frac{\sum_{i=1}^{4} c_i A_i}{\sum_{i=1}^{4} A_i} \tag{3.3}$$

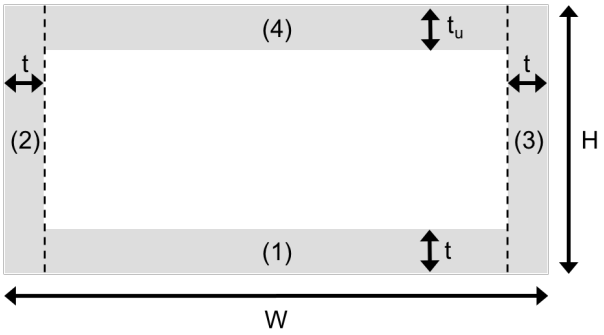

Figure 3.1: Waveguide cross section divided into sections (i=1...4) for moment of inertia calculation

The moment of inertia of each section of the smeared cross section is then determined using the parallel axis theorem:

$$\overline{I} = \sum_{i=1}^{4} \left(\frac{1}{12} b_i h_i^3 + A_i (y - c_i)^2 \right) \tag{3.4}$$

where b_i and h_i are the width and height of section i, respectively. Additionally, the mass is calculated as the volume of the waveguide material multiplied by the material density ρ:

$$M = \rho L [WH - (W - 2t)(H - t - t_u)] \tag{3.5}$$

Finally, the stresses in the top surface of the waveguide are determined using FEA with two-dimensional bilinear isoperimetric quadrilateral elements. The FEA code is adapted from plate_bliq.m, a code written by Dr. Robert Canfield for use within his FEA MATLAB toolbox. A mesh of 113 elements, shown in Figure 3.2, is generated according to the input values of d_1 and d_2. This mesh is the coarsest mesh possible, one element per slot edge. This coarse mesh is not able to take stress concentrations into account, but it avoids near-singularities that could occur with finer meshes, where the stresses would approach infinity near the corners of the slots. One end of the waveguide is fixed and a compressive force is

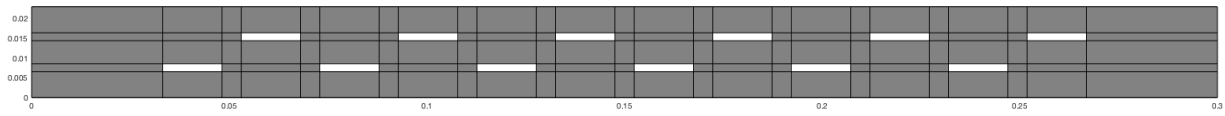

Figure 3.2: Typical waveguide upper surface membrane mesh

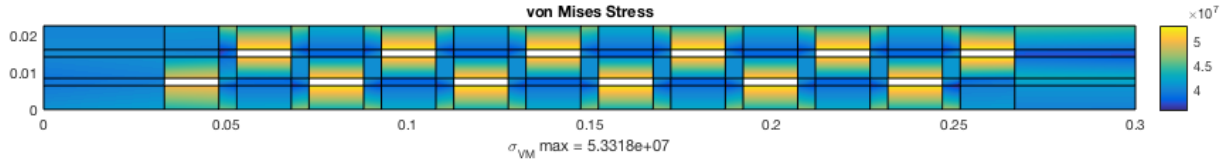

Figure 3.3: Von Mises stress distribution for the waveguide with nominal dimensions

applied along the other edge. This compressive force P is calculated by dividing the given total buckling load P_{cr} by the total perimeter of the waveguide and multiplying by the width:

$$P = \frac{P_{cr} W}{2W + 2(H - t - t_u)} \tag{3.6}$$

The three components of stress (σ_x, σ_y, and τ_{xy}) are calculated at the center of all 113 elements. Then, the von Mises stress σ_{VM} is evaluated for each element:

$$\sigma_{VM} = \sqrt{(\sigma_x - \sigma_y)^2 + \sigma_x^2 + \sigma_y^2 + 3\sqrt{2}\tau_{xy}^2} \tag{3.7}$$

The von Mises stress distribution for the nominal dimensions given in Table 2.1 is shown in Figure 3.3.

Only four design variables were used for this optimization: slot width (d_1), slot length (d_2), waveguide width (d_5), and waveguide height (d_6). The slot spacing from the centerline (d_3) and longitudinal slot spacing (d_4) are critical dimensions in electromagnetic analysis according to the sensitivity study by Ha and Canfield [13], and will be useful in a higher-fidelity structural analysis, but they do not affect the critical buckling load in this method.

These two values are therefore fixed at their nominal values.

First it is necessary to constrain the stress in the top surface of the waveguide so that it does not exceed the material yield stress before buckling. It would be simplest to only use the maximum stress value over the whole surface and create a single constraint, $\max(\sigma_{VM} < \sigma)$, however, if the element with the maximum stress changes from one iteration to another, there would be discontinuities in the gradients used for the optimization methods. Therefore, a constraint must be included for the stress in all 113 elements, leading to 113 stress constraints. While this is a significant number of constraints (versus the single constraint possible for maximum stress over the whole waveguide), it is not so many that the optimization methods cannot handle them. These stress constraints are also normalized, so they do not cause order of magnitude difficulties with the other constraints. These constraints are written as:

$$\frac{\sigma_{VM\ i}}{\sigma} - 1 < 0, \quad \text{for } i = 1, ..., 113 \tag{3.8}$$

If the mass of the waveguide were not constrained, the slots dimensions would tend towards zero and the outer waveguide dimensions would increase to their upper limits. The maximum mass is taken as that of the waveguide with the starting dimensions given in Table 3, which is denoted M_0 and is equal to 6.8534144×10^{-2} kg. The mass constraint is also normalized to avoid order of magnitude issues with the other constraints and is written as:

$$\frac{M}{M_0} - 1 < 0 \tag{3.9}$$

Lastly, a geometric constraint is necessary to prevent the slot length from exceeding the slot spacing. If the slot length were allowed to exceed the slot spacing, the mesh would have elements with negative area and would cause serious errors in the stress calculations. This constraint is normalized to prevent order of magnitude issues with the other constraints and

is written as:

$$\frac{x_2}{x_3} - 1 < 0 \tag{3.10}$$

Additionally, as a further measure to prevent the optimum solution from tending to slots of zero size and outer waveguide dimensions tending to infinity to maximize critical buckling load, some side constraints on the variables must be included. These side constraints are developed to ensure that the waveguide antenna still performs well at 10 GHz, and are the same as those used in the EM optimization in Chapter 2, where x_{lb} and x_{ub} are the lower and upper bounds on the design variables x, respectively.

The optimization of the slotted waveguides critical buckling load was performed using sequential approximate optimization (SAO) with the reciprocal approximation for the constraints[14]. For structural optimization, the reciprocal approximation is often used for the objective function as well, but that is not necessary in this case, as the objective function is exact and can be calculated analytically. This gradient-based method is appropriate in this case as the derivatives of the objective function can be analytically determined. The constraint derivatives were determined using the finite difference method. A step size study was performed and the optimal step size for taking constraint derivatives was found to be $\Delta x = 10^{-10}$ m.

The mathematical formulation of this optimization is:

$$\min_{x \epsilon \Omega} \quad -P_{cr}(x), \quad \Omega = \{x |\ \tilde{g}_R(\tilde{x}) \leq 0, \quad x_{lb} \leq x \leq x_{ub}\} \tag{3.11}$$

where Ω is the design space and $\tilde{g}_R$ are the linear approximations of the constraints in the reciprocal space. The sequential approximate optimization program makes use of sequential quadratic programming (SQP) within each iteration, to allow for each iteration of the SAO routine to find the best possible next step. The results from the SAO optimization are also compared to a pure SQP evaluation to validate the optimum.

Table 3.2: Material properties of CFRP

$\overline{E}$	Young's modulus	138.6 GPa
ρ	Density	1824 kg/m^3

3.1.2 High-Fidelity Optimization

The results from the SAO optimization of the small four-slot waveguide are given in Section 4.2.1. The results show that the analytically determined nominal values given by Wade [26] can be significantly improved upon for structural strength considerations, and the critical buckling load of a slotted waveguide may be improved with optimization. For a SWASS panel to achieve the maximum buckling strength, it follows that the individual waveguides within the panel must be optimized to have the maximum individual buckling strength possible. The waveguides that will be used in the final SWASS panel for the X-47 case study are 30 cm in length with 12 slots, as in Test Case 4 in Chapter 2, and will have the same CFRP material properties as used by Canfield and Kim [8]. These material properties are listed in Table 3.2.

The optimization in the previous section was a low-fidelity model that was designed to run as quickly as possible. However, in order to achieve accurate, usable results, the complete higher-fidelity three-dimensional FEA model with slots must be used. For this higher-fidelity model, the slot offset from centerline (d_3) and longitudinal spacing (d_4) are now considered as design variables, as in the EM optimization. Additionally, a more sophisticated optimization method was used. Because this structural optimization is to be used as part of a multi-objective design, the optimization method chosen is the same as used for the electromagnetic optimization in Chapter 2: Nelder-Mead[9]. This non-gradient-based method is an appropriate choice because the objective function may have discontinuities in it due to mode switching, if the buckling mode switches from a global buckling mode to a local buckling mode from one iteration to the next.

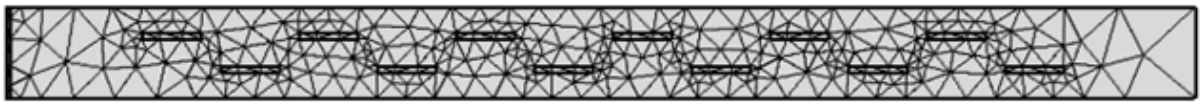

Figure 3.4: Shell mesh used for high-fidelity structural optimization

The objective function to be maximized is the same as in the previous section: critical buckling load. The objective function is evaluated using COMSOL Multiphysics, using the linear buckling analysis FEA tool with shell elements and pinned-pinned boundary conditions. The mesh, shown in Figure 3.4, is much coarser than is used for the EM analysis, due to the lower complexity of the buckling problem. However, it is a significantly finer mesh than was used for the coarse optimization in the previous section, and is able to capture the stress concentrations near the slots. As this optimization will be later be merged with the EM optimization, all of the same constraints are used, including side constraints, geometric constraints, and the mass constraint. The stress constraint is no longer explicit because the buckling calculation includes a linear analysis, from which stresses are scaled by the buckling eigenvalue for their value at incipient buckling.

3.2 Multi-Objective Optimization

The final optimization has two objectives: optimizing the EM performance and the structural strength of a 12-slot CFRP waveguide. The metric for measuring EM performance is the peak far-field gain G in decibels, as used for the EM optimization in Chapter 2. For the structural strength, the critical buckling load P_{cr} in Newtons will be evaluated using the same method as the previous section. Because the two objective functions are not in the same units or on the same magnitude, they will be normalized by the utopia point values from their respective individual optimizations (13.988 dB and 1695.5 N, respectively). The multi-

objective optimization will then attempt to maximize the sum of the normalized objectives:

$$\max_{x\epsilon\Omega}\left[\left(\frac{G(x)-14.049\text{ dB}}{14.049\text{ dB}}\right)+\left(\frac{P_{cr}(x)-1695.5\text{ N}}{1695.5\text{ N}}\right)\right],\quad \Omega=\{x|\ g(x)\leq 0,\quad x_{lb}\leq x\leq x_{ub}\} \tag{3.12}$$

where Ω is the design space, $g(x)$ are the constraints, x_{lb} and x_{ub} are the lower and upper bounds on the design variables x, respectively. The optimization will again be solved using the Nelder-Mead method with a maximum iteration count of 1000. The optimality tolerance will be set to 0.0001, meaning that the optimization will stop when an improvement of 0.0001 over the current best value of the objective function cannot be found. The total objective function is evaluated after the critical buckling load and peak far-field gain are evaluated separately using the same mesh and boundary conditions as used in the individual optimizations.

3.3 SWASS Panel Evaluation

Once the 12-slot CFRP waveguide is simultaneously optimized for maximum far-field gain and maximum critical buckling load, the performance of the entire X-47 SWASS panel will be evaluated in Chapter 5. The EM performance of the SWASS panel was determined using the same superposition process outlined in Section 2.2.3, in which the radiation pattern of the single waveguide is generated in COMSOL and superimposed using the MATLAB Phased Array Toolbox. The performance of this full SWASS panel was then be compared to a panel of waveguides with nominal dimensions, as well as commercially available weather radar antennas, and the suitability for use on the X-47 unmanned aircraft was evaluated.

Chapter 4

Results

4.1 Waveguide EM Optimization (Chapter 2 Review)

In Chapter 2, it was found that, although the far-field gain patterns for antenna arrays created using FEM and superposition appear to have significant qualitative differences, the mission-critical measures of antenna performance had relatively low error. Therefore, it was concluded that the proposed multi-fidelity method of using superposition with high-fidelity models of individual waveguides is a feasible method for modeling large waveguide arrays.

Additionally, the superposition method was compared to a high-fidelity model from the literature, where the model used for the superposition validation was modified to have ten slots and to have CFRP material properties, to better match the literature model. The individual waveguide model matched the literature model well, but the ten-waveguide array showed a larger difference in peak gain between this model and that of the literature. This may be explained by the fact that the literature model includes additional features, such as the electrical power supplies and back shorts, as well as modeling mutual interference

between the waveguides in the array.

A coarse genetic algorithm optimization was performed using on a short, perfectly conducting waveguide with four slots as a proof-of-concept to determine whether or not it would be worthwhile to proceed with a higher-fidelity and higher computation cost optimization. It was found that the result of the optimization showed significant enough improvements over the nominal dimensions to merit a more intensive optimization study.

The higher-fidelity optimization with the Nelder-Mead method was then performed, using the full 12-slot waveguide with CFRP properties, for the most realistic result possible. From the nominal dimensions, the optimum result showed a significant difference of more than 4 dB improvement over the nominal 12-slot CFRP waveguide.

Finally, a full SWASS panel array consisting of 40 12-slot CFRP waveguides with the optimal EM dimensions was modeled using the superposition method, and achieved a peak far-field gain of 35 dB. This panel will be used as a comparison point for a panel of dual-optimized waveguides.

4.2 Waveguide Structural Performance Optimization

4.2.1 Coarse Optimization Proof of Concept

The SAO method converged to an optimal critical buckling load of $P_{cr} = 1177.9$ N after 5 iterations, which is a 12.9% improvement over the nominal design, which has a critical buckling load of 1043.3 N. The resulting values of the design variables are given in Table 4.1 and the iteration history is shown in Figure 4.1a. The SQP method reached the same critical buckling load after 14 iterations. The iteration history for the SQP method is shown in Figure 4.1b. The SQP method is simpler in its execution, but is not as efficient as the

Table 4.1: Optimum values of design variables - coarse structural optimization

	Variable	Optimum Value
x_1	Slot width	0.001000 m
x_2	Slot length	0.008000 m
H	Waveguide height	0.004492 m
W	Waveguide width	0.022165 m

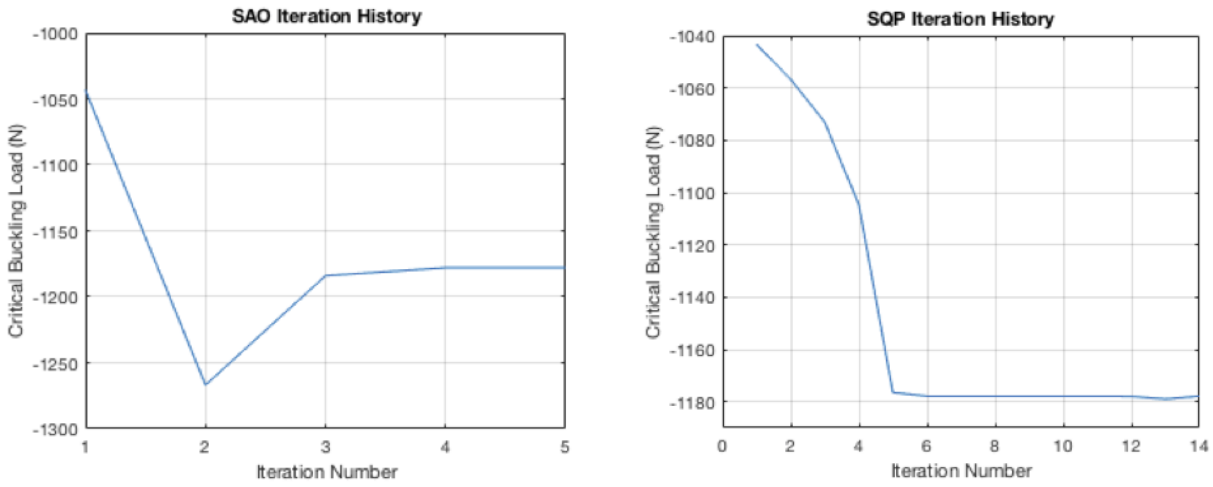

(a) (b)

Figure 4.1: Iteration history for (a) SAO and (b) SQP optimizations.

SAO method. SAO uses the reciprocal approximation for the constraints, which allows more accurate linearization of the constraints. Additionally, SAO uses SQP within each iteration to determine the next trial point, which reduces the overall number of SAO iterations that must occur.

At this optimum point, only two constraints are active: g_{22}, the von Mises stress in element 22 of the top face of the waveguide, shown in Figure 4.2, and g_{114}, the mass of the waveguide. This particular element may experience the maximum stress, rather than multiple elements in similar configurations relative to the slots, due to the non-symmetrical nature of the geometry. The mass constraint is active because, in order to maximize the critical buckling load, the moment of inertia needs to also be maximized, which means having more material

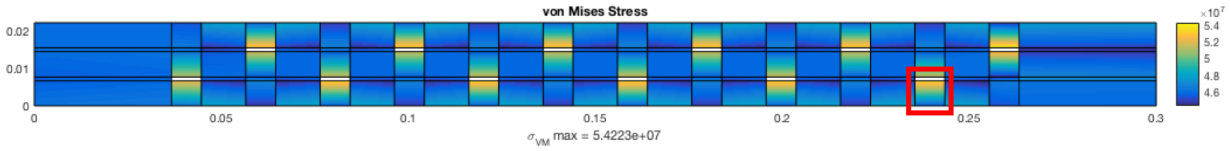

Figure 4.2: Stresses in top surface of waveguide with optimal dimensions determined by coarse optimization. Element 22 is highlighted.

in the member. The slot width and slot length were both pushed to their minimum bounds, decreasing the slot size as much as possible, as was expected. The height and width of the waveguide are not at either of their bounds, but this is due to a combination of the mass and stress constraints preventing the outer waveguide dimensions from getting too large. The design space slice for critical buckling load versus slot width and length is shown in Figure 4.3, where the height and width used are the optimum height and width. The solid black lines show the constraints and the dashed lines show the infeasible side of those constraints. All four of the constraints shown on this plot are active, and there is only the single point at the intersection of these four constraints is feasible. The maximum von Mises stress constraints are here simplified to be the maximum von Mises stress across all elements, for ease of viewing. The design space slice for critical buckling load versus waveguide width and height is shown in Figure 4.4, where the slot width and length used are the optimum slot width and length. Here the only visible constraints that are active are the maximum mass and maximum von Mises stress constraints, and the optimum is at the intersection of those constraints.

4.2.2 High-Fidelity Optimization

The Nelder-Mead optimization of the structural strength of a 12-slot waveguide with CFRP material properties converged to a solution after 104 iterations to a critical buckling load of 1695.5 N, an improvement of almost 65% over that of the waveguide with nominal dimen-

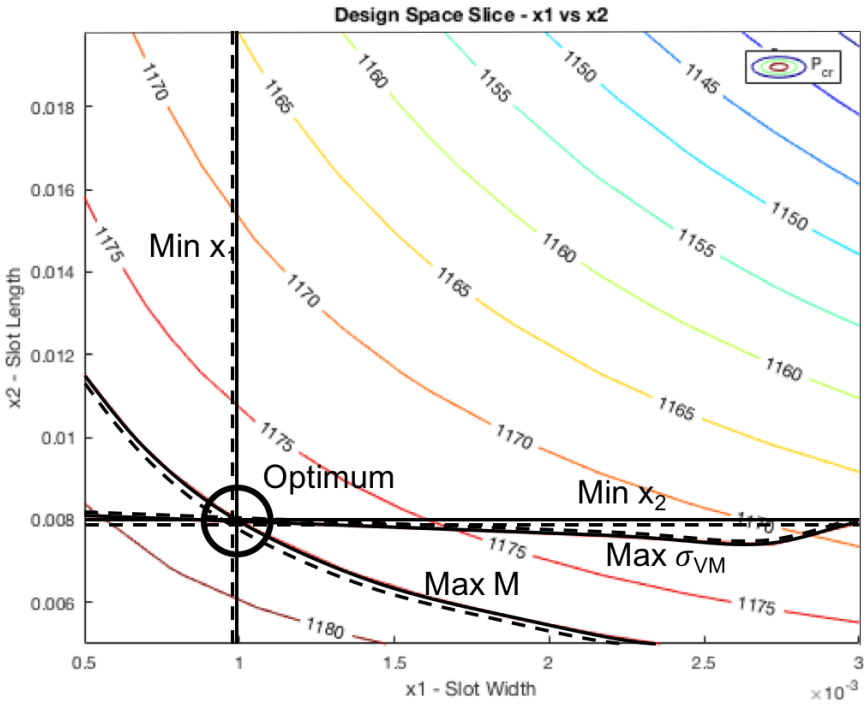

Figure 4.3: Design space slice showing critical buckling load contours versus slot width and length

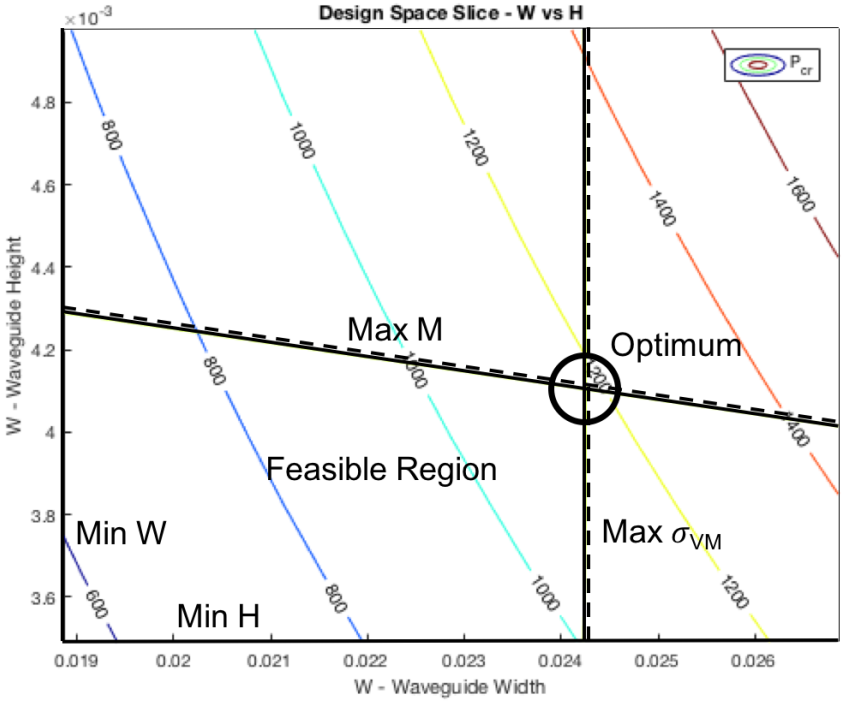

Figure 4.4: Design space slice showing critical buckling load versus waveguide width and height

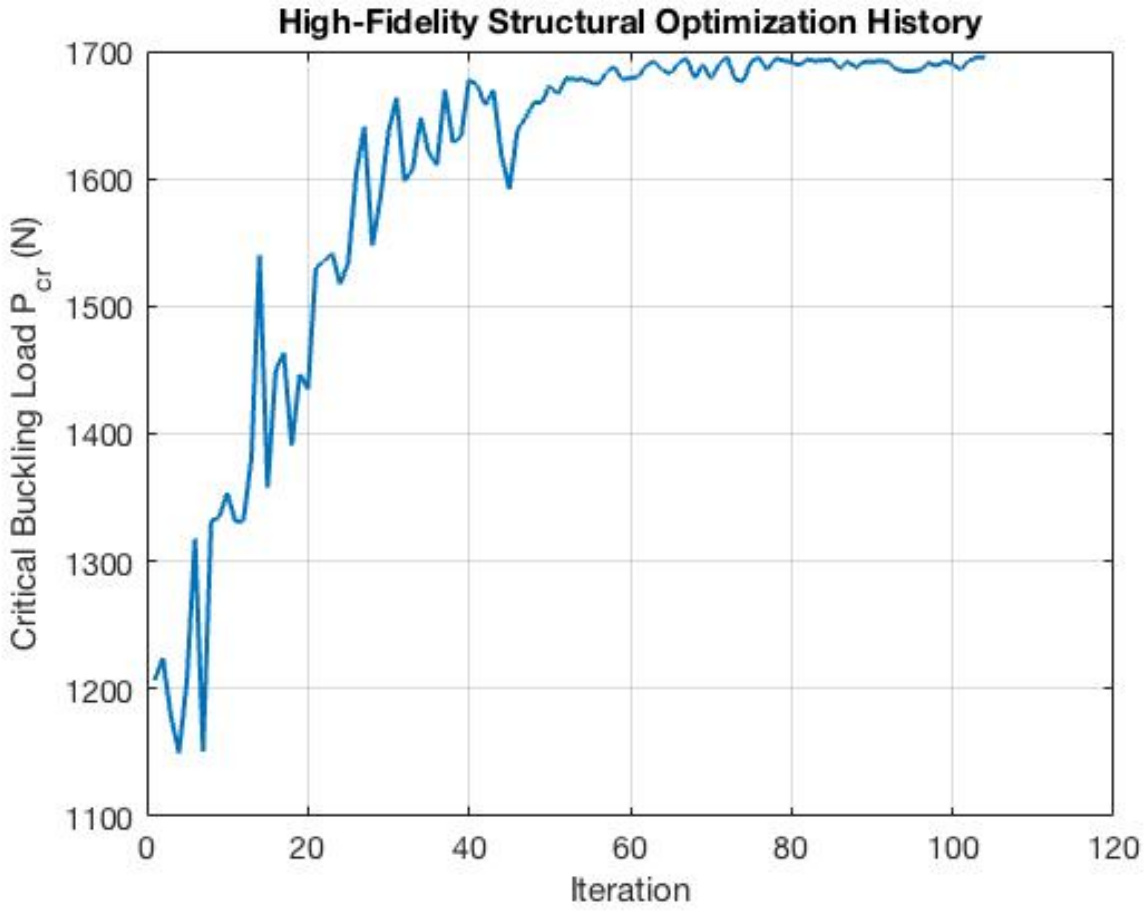

Figure 4.5: Iteration history for high-fidelity structural optimization

sions, which had a critical buckling load of only 1028 N. The convergence history for the optimization is shown in Figure 4.5. The waveguide dimensions that result in the optimum peak far-field gain are shown alongside the nominal dimensions in Table 4.2. A geometric comparison of the nominal and optimal waveguide models is shown in Figure 4.6. It is visually evident that the slots have decreased in size and have spread out to allow more area between them, which decreases the stress concentration. Additionally, the width of the waveguide has been sacrificed to increase the height, allowing the cross-sectional moment of inertia to increase. These three qualitative changes result in a stiffer waveguide with a significantly higher critical buckling load.

Table 4.2: Optimum Slotted Waveguide Dimensions - High-Fidelity Structural Optimization

Variable	Description	Nominal Value	Optimum Value	Difference
d_1	Slot width	1.59 mm	1.780 mm	+11.9%
d_2	Slot length	14.84 mm	11.538 mm	−22.3%
d_3	Slot offset from centerline	4.22 mm	2.095 mm	−50.4%
d_4	Longitudinal slot spacing	19.88 mm	18.961 mm	−4.6%
d_5	Waveguide width	22.86 mm	18.860 mm	−17.5%
d_6	Waveguide height	10.16 mm	11.940 mm	+17.5%
G	Peak far-field gain	9.65 dB	14.05 dB	+4.40 dB
P_{cr}	Critical buckling load	1028.0 N	1341.5 N	+30.5%

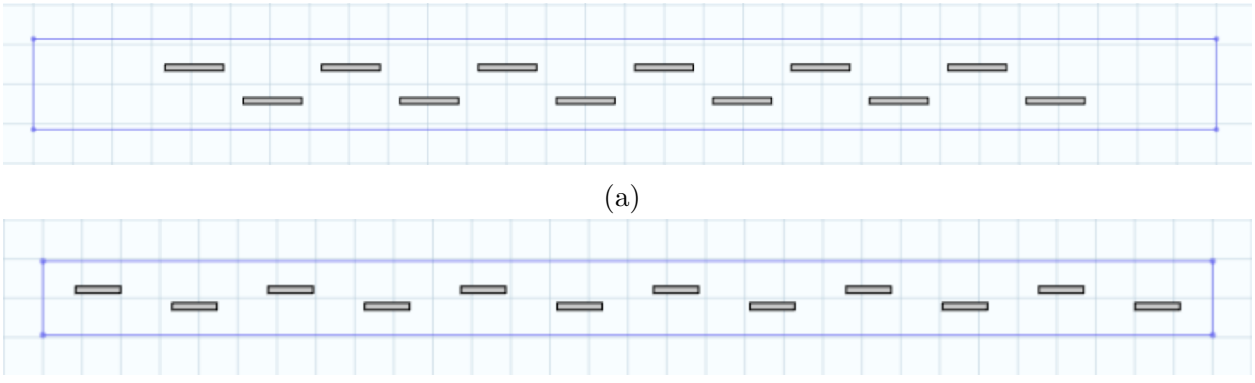

(a)

(b)

Figure 4.6: (a) Nominal and (b) structurally optimal waveguide configurations

4.3 Multi-Objective Optimization

The Nelder-Mead multi-objective optimization of the 12-slot waveguide with CFRP material properties converged to a solution after 121 iterations to a peak far-field gain of 13.92 dB and critical buckling load of 1476.98 N. The iteration history for the far-field gain and buckling load is shown in Figure 4.7. The sum of objectives history is shown in Figure 4.8. The resulting waveguide dimensions are shown alongside the nominal dimensions in Table 4.3. A geometric comparison of the nominal and optimal waveguide models, as well as the individually optimized models, is shown in Figure 4.9.

This multi-objective optimization resulted in a peak gain sacrifice of only 0.13 dB from the EM optimum of 14.05 dB, but an increased buckling load of 135 N over the EM optimum configuration (1341.5 N). From the perspective of the structural optimization, this results in a sacrificed 220 N from the critical load of 1695.5 dB, while increasing the far-field gain by 5.29 dB (from 8.6338 N). In both cases, the results of this multi-objective optimization are significant improvements over the nominal configuration. The EM performance increased by 4.27 dB over that of the nominal configuration, which had a peak gain of 9.65 dB. The structural strength improved by 44% over the nominal configuration, which had a critical buckling load of 1028 N.

The far-field gain patterns for the dual-optimized 12-slot CFRP waveguide are compared with the nominal configuration gain patterns in Figure 4.10. The qualitative differences are slight, but it is possible to see that the main lobe of the optimized configuration pattern is slightly more concentrated than that of the nominal configuration, and the side lobes show less red and orange (higher gain areas). Quantitatively, it is evident that the peak gain and overall gain of the optimized antenna is significantly higher.

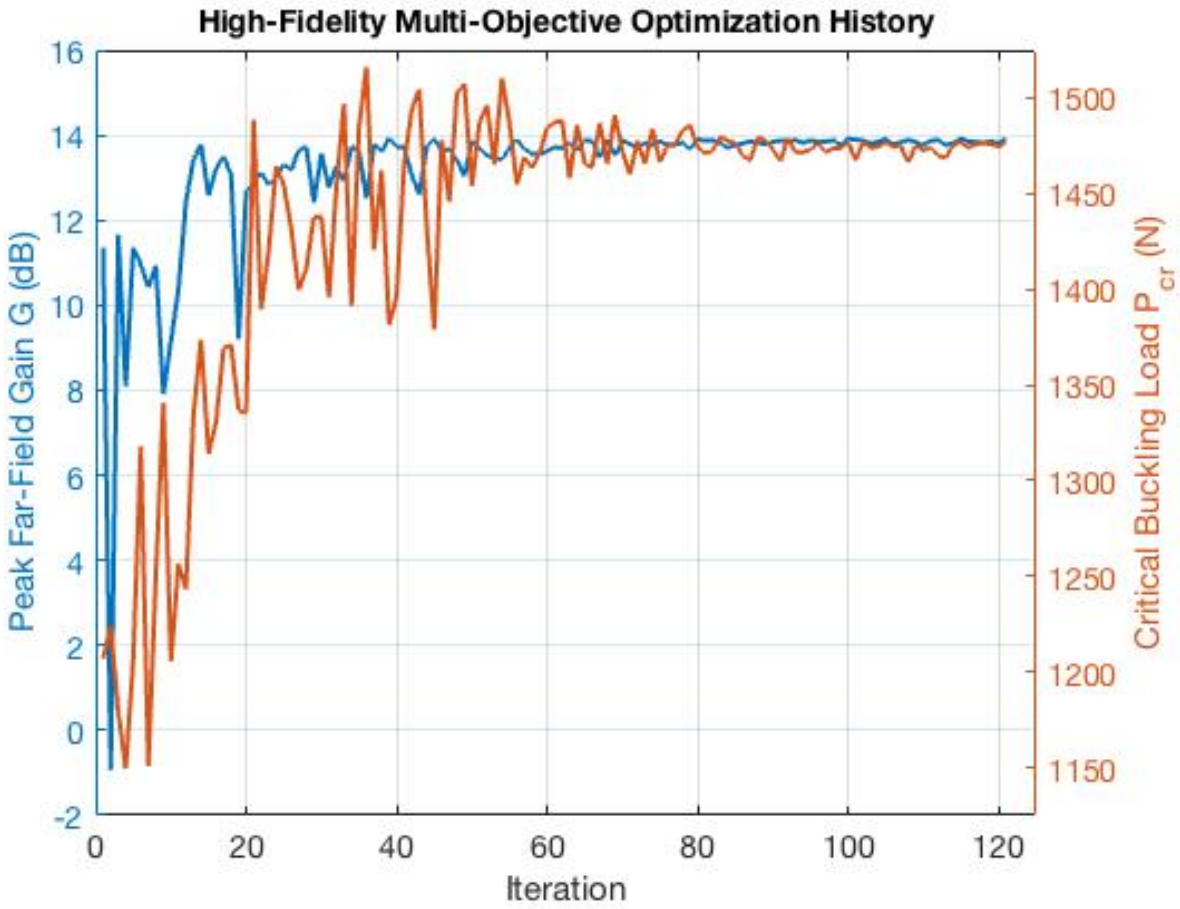

Figure 4.7: Multi-Objective Optimization Iteration History

Table 4.3: Optimum Slotted Waveguide Dimensions - Multi-Objective Optimization

Variable	Description	Nominal Value	Optimum Value	% Difference
d_1	Slot width	1.59 mm	3.000 mm	+88.7%
d_2	Slot length	14.84 mm	12.657 mm	−14.7%
d_3	Slot offset from centerline	4.22 mm	2.560 mm	−39.3%
d_4	Longitudinal slot spacing	19.88 mm	19.173 mm	−3.5%
d_5	Waveguide width	22.86 mm	20.388 mm	−11.8%
d_6	Waveguide height	10.16 mm	11.511 mm	+13.3%
G	Peak far-field gain	9.65 dB	13.92 dB	+4.27 dB
P_{cr}	Critical buckling load	1028.0 N	1477 N	+43.7%

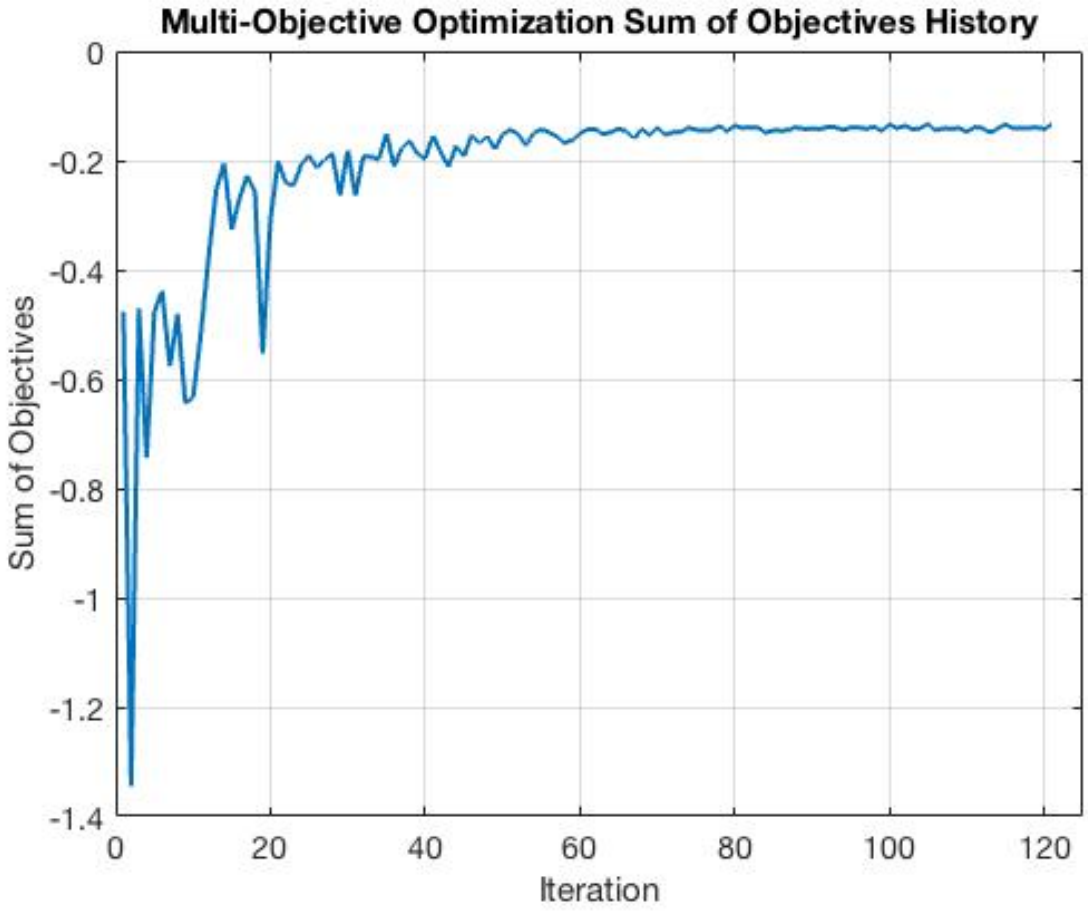

Figure 4.8: Multi-Objective Optimization Objective Function History

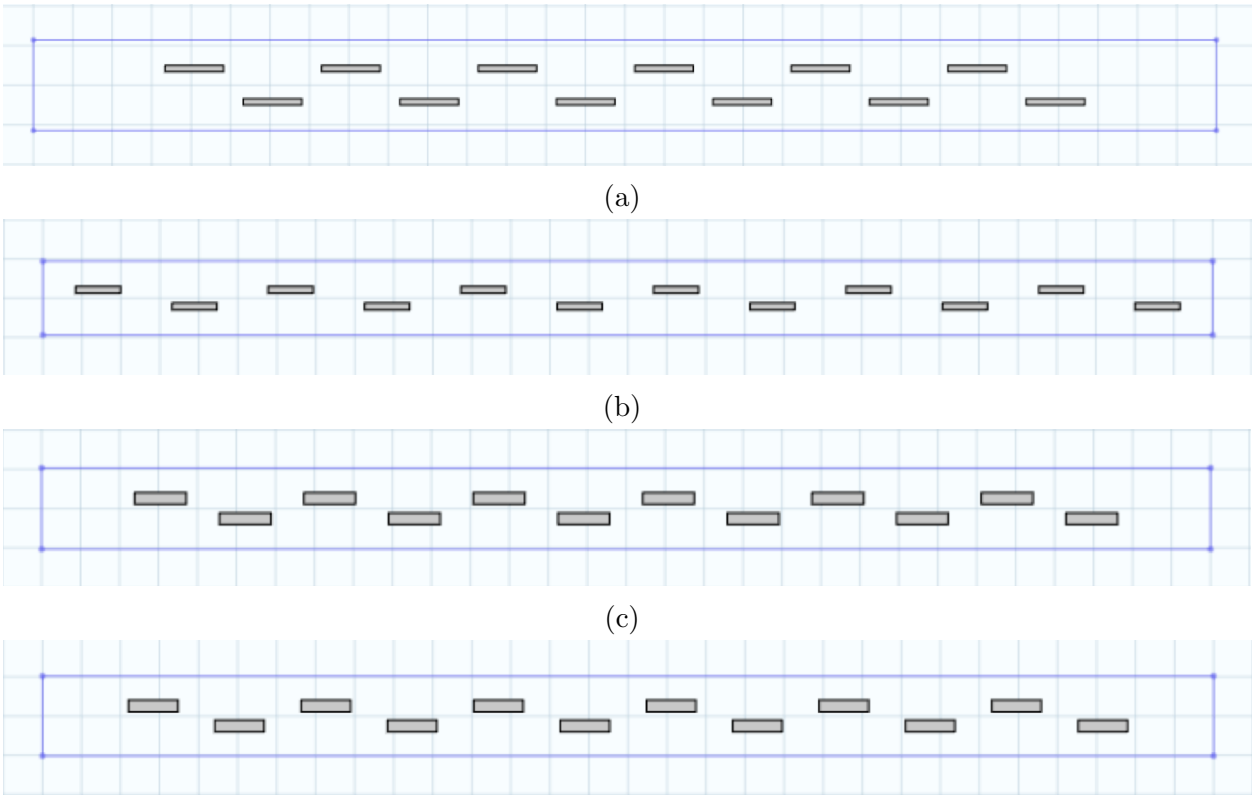

(a)

(b)

(c)

(d)

Figure 4.9: (a) Nominal, (b) structurally optimized, (c) EM optimized, and (d) dual-optimized waveguide configurations

4.4 SWASS Panel Evaluation

An antenna array consisting of 40 WR-90 slotted waveguide antennas arranged linearly side by side forms a panel of approximately 1 m × 0.3 m. A panel of this size could easily replace one of the panels on the wing of an X-47 aircraft, to be used as a weather radar system. The optimized waveguide model developed in the previous section was imported to the Phased Array Toolbox for superposition in a 40-element array. The peak far-field gain for the dual-optimized array was 34.34 dB, as compared with 32.74 dB for the nominal array, a difference of 1.60 dB. The array of dual-optimized waveguides has a peak far-field gain of just 0.58 dB less than that of the electromagnetically optimized array in Chapter 2, which had a peak gain of 34.92 dB.

The array gain pattern from this array is compared with an array consisting of waveguides with nominal dimensions is shown in Figure 4.11. As with the arrays of electromagnetically optimized and nominal waveguides, the array of structurally and electromagnetically optimized waveguides shows a great number of side lobes on the side view, corresponding roughly to one additional side lobe per waveguide. It is evident from a visual inspection of the front view patterns that the energy in the optimized array is more focused, as the lobes are more defined and distinct.

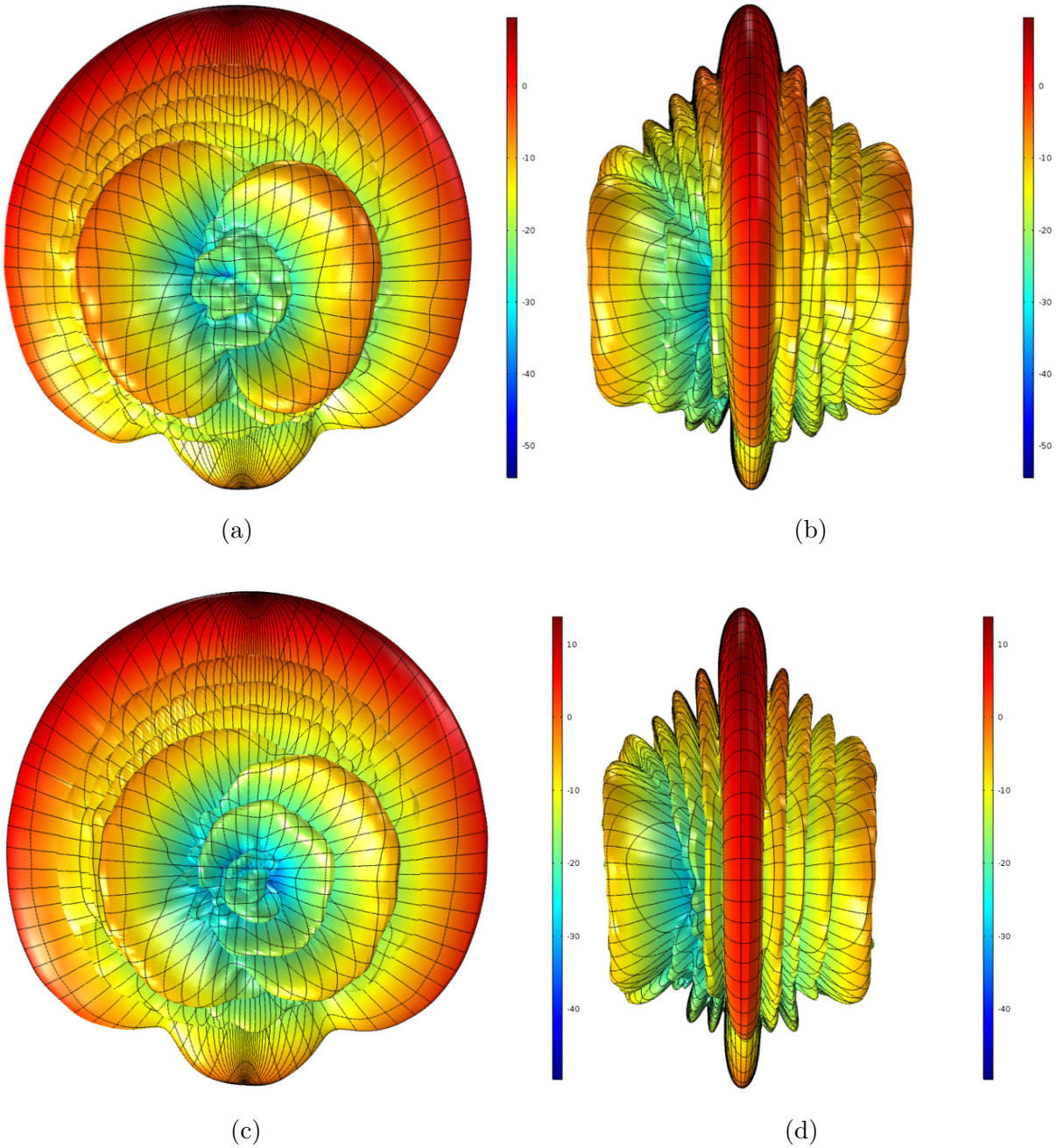

Figure 4.10: Far-field gain (dB) patterns before and after high-fidelity multi-objective optimization. Waveguide with nominal dimensions (a) front and (b) side views. Waveguide with dual-optimized dimensions (c) front and (d) side views.

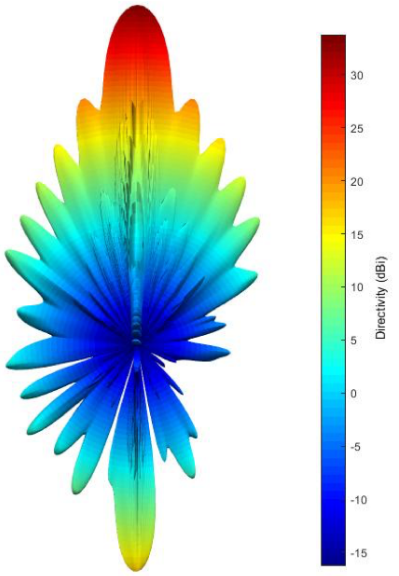

(a)

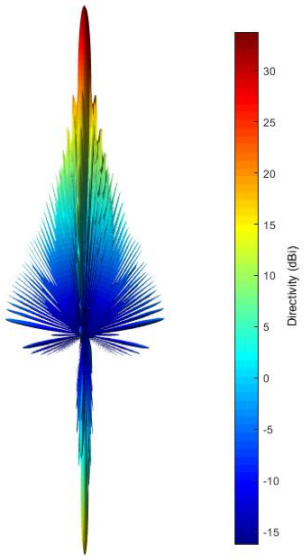

(b)

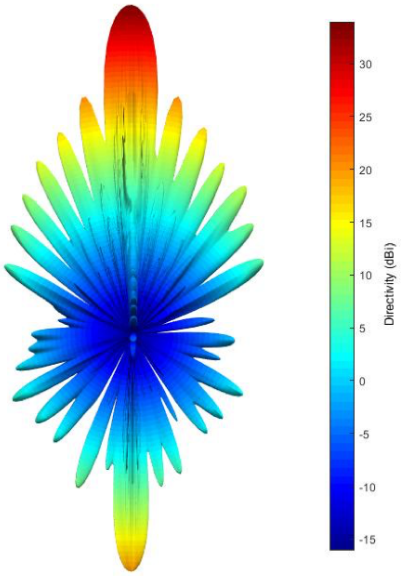

(c)

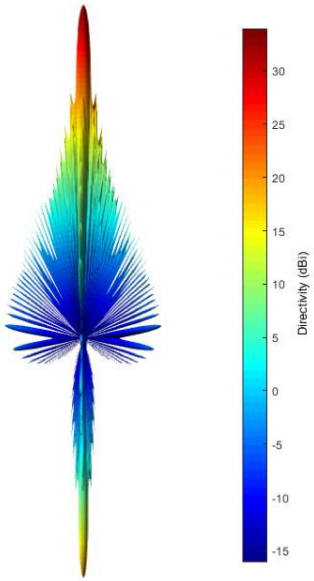

(d)

Figure 4.11: 40-waveguide SWASS array far-field gain (dB) patterns before and after high-fidelity multi-objective optimization. Array consisting of waveguides with nominal dimensions (a) front and (b) side views. Array of optimized waveguides (c) front and (d) side views.

Chapter 5

Conclusions & Summary

In Chapter 2, a computationally low-cost method for modeling large waveguide arrays was developed. Calculating the far-field gain of a waveguide using FEM requires meshing the entire sphere of space around the waveguide, in addition to meshing the waveguide itself. This means that as waveguide length or number of waveguides increases, the number of degrees of freedom in the FEM calculation grows cubically. This prohibits modeling larger arrays without using distributed computing or other types of supercomputers, so superposition, which is much less computationally expensive, may be used to model large arrays. Using several test cases, this process was verified to have low peak far-field gain error, side lobe far-field gain error, and lobe angular error.

To provide a more realistic model, the perfect electrical properties were changed to be real values for CFRP material. The implementation of these material properties was verified and the superposition process was again verified against CFRP waveguide values determined experimentally. The peak far-field gain from the single waveguide matched almost perfectly with the literature value. However, the array peak gain was off by a few decibels, which may be due to the fact that the power supply, backshort, and mutual interference are modeled in

the literature and are not modeled here.

A coarse genetic algorithm optimization was performed on a short four-slot waveguide as a proof-of-concept step to see if the peak far-field gain could be improved by modifying Elliott's values. A modest improvement was seen, so the full-scale high-fidelity optimization was performed using the Nelder-Mead method on a larger 12-slot waveguide with realistic CFRP electrical properties. This optimization resulted in a peak far-field gain of 14.05 dB, an improvement of 4.40 dB over the nominal configuration gain of 9.65 dB.

This optimized waveguide far-field gain pattern was then used in the validated superposition method to create an electromagnetic model of approximately the same size as a wing panel on a Northrop-Grumman X-47 unmanned aircraft. This panel consisted of 40 WR-90 waveguide elements of length 30 cm, resulting in a panel with dimensions of 1 m by 0.3 m. The peak far-field gain of this panel was found to be 34.92 dB, 2.18 dB greater than that of an array of the same size with waveguides of nominal dimensions, which was 32.74 dB. A difference of 2.18 dB seems small at first glance, but given that decibels are on a log scale, the optimized SWASS panel has a peak far-field gain of more than 65% greater than that of the nominally dimensions SWASS panel.

After electromagnetic optimization had been achieved, the next step was including some structural strength considerations. Initially, another coarse proof-of-concept optimization was performed, this time for the critical buckling load using the SAO method with reciprocal constraints, to see if an improvement could be made to the strength of a waveguide by adjusting the slot and waveguide sizes. It was determined that an improvement over the nominal dimensions could be found, so a higher-fidelity optimization with realistic CFRP material properties was completed using the same method as in Chapter 2 for the EM optimization. This optimization was able to improve the critical buckling load to 1695.5 N, an improvement of 667.5 N over the nominal waveguide, which had a critical buckling load

Table 5.1: Comparison of three optimized configurations with nominal configuration

	Nominal	EM Optimized	Structurally Optimized	Dual-optimized
G (dB)	9.65	14.05	8.63	13.92
P_{cr} (N)	1028.0	1341.5	1695.5	1477.0

of 1028 N. For reference, the EM optimum configuration found in Chapter 2 results in a buckling load of 1341.5 N, which is still a significant improvement over the nominal.

One final optimization was required to determine a balance between the structural and electromagnetic strength, to ensure that the final SWASS panel would be able to fulfill all mission requirements. Using the same Nelder-Mead method with the same constraints, a sum of objectives optimization was performed, using the normalized utopia points from the high-fidelity structural and EM optimizations as the objectives. The optimal balance between the structural strength and EM performance was found to be 1477.0 N critical buckling strength and 13.92 dB peak far-field gain. A summary of the three high-fidelity optimizations versus the nominal configuration is given in Table 5.1.

Next, a full-size SWASS array panel was modeled with the superposition method outlined in Chapter 2, using the dual-optimized waveguide. The peak far-field gain of this array was found to be 34.34 dB, an improvement of 1.6 dB (45%) over the nominal SWASS panel, which had a peak gain of 32.74 dB. Considering that the critical buckling load of the dual-optimized waveguide is 44% higher than that of the nominal waveguide, this could be considered to be a highly successful balance between electromagnetic and structural performance.

Lastly, the performance of this SWASS panel must be compared to that of a commercially available slotted waveguide array antenna that this SWASS panel might replace. The RDR 2000 Digital Weather Radar System manufactured by Honeywell will be used as a typical weather radar system for this comparison [2]. The RDR 2000 is a mechanically-steered

waveguide array antenna that is intended to be mounted inside the nose cone radome of a small craft of a similar size to the Northrop-Grumman X-47 unmanned aircraft. The literature for this product states that the peak far-field gain of the RDR 2000 is 30 dB (other similar systems are near this level of gain, ±2 dB). Therefore, it can be concluded that the 1 m × 0.3 m SWASS panel made up of 40 12-slot CFRP waveguide antennas with the slot and waveguide dimensions as found by the multi-objective optimization is capable of meeting or exceeding the EM mission requirements.

SWASS present a few disadvantages when compared to traditionally mechanically steered radar antennas. Due to the fact that the waveguides are embedded within the skin of the aircraft, maintenance could be problematic as accessing the waveguides is not as easy as with a removable radome. However, if the SWASS panel constitutes an entire skin panel, it is possible that the skin panel may be removed and switched out with a functioning SWASS panel while the damaged panel is repaired. Another issue deals with beam steering, as weather radar must be able to scan within a certain area in front of the aircraft. For traditional antennas like the RDR 2000, this is easily accomplished by simply rotating the entire antenna using mechanical servos. With SWASS, the radar beam must be electrically steered using phase shifting, which is a significantly more complex problem. While this can lead to some interesting effects with the side lobes, the peak far-field gain remains almost constant. However, the weight and drag savings gained by the implementation of SWASS would be worth the additional effort put into programming the electrical steering. If the beam is not able to be steered enough to both sides by a single panel in one wing, two panels may be used, one on each wing. The electrical phase shift beam steering used by SWASS is actually beneficial for a radar system, especially in military applications. The mechanically steered antenna has to physically reorient itself to steer the beam, where it is subject to the speed of the servos and to its own inertia. This limits the ability for such an antenna to

respond to quickly moving targets, or to track multiple targets at once. The electrical beam steering of a SWASS panel has near-infinite beam steering speed, so by alternating back and forth, it is able to track multiple targets. This is not as much of a concern with weather radar, as is used in the case study in this thesis, but SWASS could also be used for enemy fighter jet or missile tracking.

5.1 Summary of Technical Contributions

The main objective of this research was to aid the future implementation of SWASS by reducing the need for computationally expensive high-fidelity analyses with a new multi-fidelity design method. This method was intended to be used in the case study to evaluate the possibility of using SWASS as weather radar on the Northrop-Grumman X-47 unmanned aircraft. The goals of this research were met by proposing and validating a multi-fidelity electromagnetic design method for SWASS panels, determining an optimum set of waveguide dimensions to produce a structurally strong waveguide with high far-field gain, and lastly to model a full SWASS panel for use in the X-47 aircraft with the optimum structural and EM characteristics. All three of these goals were met.

The multi-fidelity modeling method presented here can be used as a computationally lower cost method of verifying SWASS designs for airworthiness. The time and computational power required for a fully high-fidelity full panel optimization would be prohibitive, especially in the early design phase. Once the RF radiation pattern for a single waveguide antenna is evaluated using the high-fidelity solver (a process that takes several minutes), the reduced computational effort of superposition allows modeling the RF radiation pattern of an entire array in a matter of seconds.

5.2 Recommendations for Future Work

The electromagnetic optimization of the SWASS array panel may be improved in the future by performing the superposition calculation at every iteration and using the peak far-field gain of the entire panel as the objective function, instead of just that of a single waveguide. This would significantly increase the solution time, but it may be that the additive and subtractive interference in the superposition calculation may result in a different set of waveguide dimensions that produces a greater peak far-field gain for the whole panel. Additionally, future work is needed to improve the fidelity of the high-fidelity model, such as by including models of the power supply and backshort.

In-depth analysis of the structural performance of entire SWASS arrays will be left for future work. In this research, only the global buckling mode of a single waveguide was considered, but in reality, a SWASS panel would behave more like a plate than a set of individually acting slender members. Additionally, the boundary conditions on the plate would be fastened around the entire perimeter, instead of just at the ends. The treatment of a SWASS panel as a plate with pinned boundary conditions would likely have a higher structural strength than what is estimated by superposition of single waveguides. A complete buckling analysis of this SWASS panel could then be used as the objective function for the structural analysis half of the dual optimization, leading to a higher-fidelity result than what was obtained here.

Bibliography

[1] Nicholas J Albertson and Robert A Canfield. Electromagnetic modeling of large phased arrays of structurally embedded waveguides. In *58th AIAA/ASCE/AHS/ASC Structures, Structural Dynamics, and Materials Conference, AIAA SciTech Forum*. AIAA, 2017. doi: 10.2514/6.2017-0428.

[2] *Digital Weather Radar System Pilot's Guide*. Allied Signal Inc., 1998. https://www.nifc.gov/aviation/BLMsmkjAC/Radar_UG.pdf.

[3] K.H. Alt, A.J. Lockyer, D.P. Coughlin, J.N. Kudva, and J. Tuss. Overview of the dod's rf multifunction structural aperture (mustrap) program. *Smart Structures and Materials 2001: Smart Electronics and MEMS*, 2001.

[4] Nicholas A Bishop, Jason Miller, David Zeppettella, William Baron, James Tuss, and Mohammod Ali. A Broadband High-Gain Bi-Layer LPDA for UHF Conformal Load-Bearing Antenna Structures (CLAS) Applications. *IEEE Transactions on Antennas and Propagation*, 63(5):2359–2364, 2015. ISSN 0018926X. doi: 10.1109/TAP.2015.2409866.

[5] Paul J. Callus. Conformal Load-Bearing Antenna Structure for Australian Defence Force Aircraft. Technical report, Defence Science and Technology Organization, Australia, 2007.

[6] Paul J Callus. Novel Concepts for Conformal Load-bearing Antenna Structure. Technical report, Defence Science and Technology Organization, Australia, 2008.

[7] Paul J Callus, Kelvin J Nicholson, and Alexe Bojovschi. A Planar Antenna Array Manufactured From Carbon Fibre Reinforced Plastic. *28th International Congress of the Aeronautical Sciences, Brisbane, Australia*, 2012.

[8] Robert Canfield and Woon Kim. AFRL-VT-WSU Collaborative Center on Multidisciplinary Sciences - Design Optimization of Slotted Waveguide Antenna Stiffened Structures (SWASS). Technical Report 540, 2014. URL http://hdl.handle.net/10919/47360.

[9] COMSOL. *COMSOL Multiphysics Reference Guide*. 2012. ISBN 1781273332.

[10] R. S. Elliott. *Antenna Theory and Design*, pages 17–26. IEEE-Wiley, 2003.

[11] Robert S. Elliott. An Improved Design Procedure for Small Arrays of Shunt Slots. *IEEE Transactions on Antennas and Propagation*, 31(1):48–53, 1983. ISSN 15582221. doi: 10.1109/TAP.1983.1143002.

[12] Estqwerty. 5 ghz slotted waveguide, 2007. Online. http://www.digdice.com/2007/11/5ghz-slotted-waveguide/.

[13] Taekwang Ha and Robert Canfield. Design Optimization of a WR-90 Slotted Waveguide Antenna Stiffened Structures. *52nd AIAA/ASME/ASCE/AHS/ASC Structures, Structural Dynamics and Materials Conference, Denver, Colorado, April 4-7*, 2011. doi: 10.2514/6.2011-2147.

[14] Raphael T. Haftka and Zafer Gürdal. *Elements of Structural Optimization*. Kluwer Academic Publishers, 3rd revised and expanded edition edition, 1992.

[15] Woon Kim, Robert A Canfield, William Baron, James Tuss, and James Miller. Modeling and Simulation of Slotted Waveguide Antenna Stiffened Structures. *The 19th International Conference on Composite Materials, Montreal, Canada*, pages 2012–2019, 2013.

[16] A Lockyer, K Alt, D Coughlin, M Durham, J Kudva, A Goetz, and J Tuss. Design and development of a conformal load-bearing smart-skin antenna: overview of the afrl smart skin structures technology demonstration (s3td). *Smart Structures and Materials 1999: Industrial and Commercial Applications of Smart Structures Technologies*, 1999.

[17] Mathworks. *MATLAB Phased Array System Toolbox User's Guide*. 2016.

[18] Mathworks. *MATLAB Global Optimization Toolbox User's Guide*. 2017.

[19] NASA. Airborne weather radar nasa, 2009. URL https://commons.wikimedia.org/wiki/File:Airborne_weather_radar_NASA.jpg. Online. https://commons.wikimedia.org/wiki/File:Airborne_weather_radar_NASA.jpg.

[20] NASA. Nasa completes ads-b flight evaluations for uas, 2012. URL https://www.nasa.gov/centers/dryden/Features/ads-b_tests_complete.html. Online. https://www.nasa.gov/centers/dryden/Features/ads-b_tests_complete.html.

[21] NATO. Awacs: Nato's 'eyes in the sky', 2017. URL https://www.nato.int/cps/en/natohq/topics_48904.htm. Online. https://www.nato.int/cps/en/natohq/topics_48904.htm.

[22] Northrup Grumman. X-47B UCAS, 2015. URL http://www.as.northropgrumman.com/products/nucasx47b/index.html. Online. http://www.as.northropgrumman.com/products/nucasx47b/index.html.

[23] Ben Smallwood, Robert Canfield, and Andrew Terzuoli. Structurally Integrated Antennas on a Joined-Wing Aircraft. *44th AIAA/ASME/ASCE/AHS/ASC Structures, Structural Dynamics, and Materials Conference*, April 2003. doi: doi:10.2514/6.2003-1459. URL http://dx.doi.org/10.2514/6.2003-1459.

[24] Warren L. Stutzman and Gary A. Thiele. *Antenna Theory and Design, Third Edition*. Wiley, 2012. ISBN 9788578110796. doi: 10.1017/CBO9781107415324.004.

[25] Manny Urcia and David Banks. Structurally integrated phased arrays. *IEEE Aerospace Conference 2011*, pages 1–8, 2011. ISSN 1095323X. doi: 10.1109/AERO.2011.5747321. URL http://ieeexplore.ieee.org/xpls/abs{_}all.jsp?arnumber=5747321{&}tag=1.

[26] Paul Wade. Slot Antennas. In *W1GHZ Online Microwave Antenna Book*, chapter 7. 2001. URL http://www.qsl.net/n1bwt. Online. http://www.qsl.net/n1bwt.